AFRL-AFOSR-VA-TR-2022-0571

Examining Growth of Turbulence over Heated Walls in Hypersonic Flows

Veeraragavan, Anand
THE UNIVERSITY OF QUEENSLAND
UNIVERSITY OF QUEENSLAND
BRISBANE, , 4072
AUS

08/25/2022
Final Technical Report

Air Force Research Laboratory
Air Force Office of Scientific Research
Arlington, Virginia 22203
Air Force Materiel Command

REPORT DOCUMENTATION PAGE

PLEASE DO NOT RETURN YOUR FORM TO THE ABOVE ORGANIZATION.

1. REPORT DATE	2. REPORT TYPE	3. DATES COVERED	
20220825	Final	START DATE 20180715	END DATE 20220114

4. TITLE AND SUBTITLE
Examining Growth of Turbulence over Heated Walls in Hypersonic Flows

5a. CONTRACT NUMBER	5b. GRANT NUMBER	5c. PROGRAM ELEMENT NUMBER
	FA9550-18-1-0265	61102F
5d. PROJECT NUMBER	**5e. TASK NUMBER**	**5f. WORK UNIT NUMBER**

6. AUTHOR(S)
Anand Veeraragavan

7. PERFORMING ORGANIZATION NAME(S) AND ADDRESS(ES)
THE UNIVERSITY OF QUEENSLAND
UNIVERSITY OF QUEENSLAND
BRISBANE 4072
AUS

8. PERFORMING ORGANIZATION REPORT NUMBER

9. SPONSORING/MONITORING AGENCY NAME(S) AND ADDRESS(ES)	10. SPONSOR/MONITOR'S ACRONYM(S)	11. SPONSOR/MONITOR'S REPORT NUMBER(S)
Air Force Office of Scientific Research 875 N. Randolph St. Room 3112 Arlington, VA 22203	AFRL/AFOSR RTA1	AFRL-AFOSR-VA-TR-2022-0571

12. DISTRIBUTION/AVAILABILITY STATEMENT
A Distribution Unlimited: PB Public Release

13. SUPPLEMENTARY NOTES

14. ABSTRACT
Reflected shock tunnels can reproduce realistic pressures, speeds, and temperatures of atmospheric hypersonic flight, however, their short test time does not allow the structure of the models to thermally equilibrate to the temperatures that flight models experience. This project, therefore, fulfilled this gap via designing a heated flat plate model in order to overcome this limitation and leverage the notable flight-matched test capabilities of reflected shock tunnel hypersonic flow experiments. In year 1 of this project, it was aimed for the test model to reliably and rapidly achieve flight-realistic wall temperatures in the T4 free-piston driven shock tunnel at the University of Queensland. This was achieved using a rectangular graphite plate that was electrically heated to temperatures above 800K. The design of the heated model involved careful planning around safety, and ensuring that the support structures did not cause the plate to warp or bend when heating was applied and yet hold it firmly in place during the hypersonic tests. The design was rigorously assessed by a local team of experts from a safety perspective prior to the first vacuum/ Infrared thermography was employed to measure the surface temperature immediately before a test. Visualized flow-fields from schlieren imaging showed that the heated wall conditions made a significant difference in the growth of the boundary layer, and showed that the heated wall accelerated the boundary layer transition in hypersonic flows.

15. SUBJECT TERMS

16. SECURITY CLASSIFICATION OF:			17. LIMITATION OF ABSTRACT	18. NUMBER OF PAGES
a. REPORT	b. ABSTRACT	c. THIS PAGE		
U	U	U	UU	55

19a. NAME OF RESPONSIBLE PERSON	19b. PHONE NUMBER *(Include area code)*
SARAH POPKIN	000-0000

UQ/AFOSR - Examining Growth of Turbulence Over Heated Walls in Hypersonic Flows

Final Report: Development of Heated Model, CFLDI and Test Results

Project Number: FA9550-18-1-0265

Program Manager: Dr. Sarah Popkin

A/Prof. Anand Veeraragavan, Principal Investigator
A/Prof. Vincent Wheatley, Co-Investigator
Mr. Eric Chang and Mr. Keill Hopkins, PhD Students

Centre for Hypersonics

The University of Queensland

22nd August 2022

ABSTRACT

Reflected shock tunnels can reproduce realistic pressures, speeds, and temperatures of atmospheric hypersonic flight, however, their short test time does not allow the structure of the models to thermally equilibrate to the temperatures that flight models experience. This project, therefore, fulfilled this gap via designing a heated flat plate model in order to overcome this limitation and leverage the notable flight-matched test capabilities of reflected shock tunnel hypersonic flow experiments.

In year 1 of this project, it was aimed for the test model to reliably and rapidly achieve flight-realistic wall temperatures in the T4 free-piston driven shock tunnel at the University of Queensland. This was achieved using a rectangular graphite plate that was electrically heated to temperatures above 800K. The design of the heated model involved careful planning around safety, and ensuring that the support structures did not cause the plate to warp or bend when heating was applied and yet hold it firmly in place during the hypersonic tests. The design was rigorously assessed by a local team of experts from a safety perspective prior to the first vacuum/ Infrared thermography was employed to measure the surface temperature immediately before a test. Visualized flow-fields from schlieren imaging showed that the heated wall conditions made a significant difference in the growth of the boundary layer, and showed that the heated wall accelerated the boundary layer transition in hypersonic flows.

In year 2, we focused on the development of the optical diagnostics needed for assessing the growth of turbulence in the hypersonic boundary layer. For this, we chose an unheated but instrumented (with surface pressure/heat transfer sensors) model which was tested under similar conditions to the heated model tests from Year 1. These studies focused on demonstrating that the surface heat transfer measurements (cast as dimensionless Stanton number measurements) matched the expected laminar and turbulent heat transfer levels in the respective regimes with a clearly demarcated transition region and also allowed the development and testing of the Cylindrical Focused Laser Differential Interferometry (CFLDI) technique to make turbulence measurements in the boundary layer. As expected, increasing the unit Reynold's number of the flow delayed the onset of transition. Boundary layer trips were also utilized to investigate if the heat transfer measurements showed any "memory effect" of tripping. Surface roughness elements have been used to overcome the large prediction uncertainties of hypersonic boundary layer transition. They provide the ability to force transition at short distances downstream from the tripping element to ensure turbulent boundary layers are present. This is useful on vehicle surfaces where a laminar boundary layer could produce separation bubbles heavily affecting the flow field, as well as in ground test facilities that do not have the space to allow for natural transition to occur. A large number of investigations have looked into the effects that the shape and size of a boundary layer trip has on the transition location. However, few have investigated the effect that trips have on downstream boundary layer turbulence. Our surface measurements did not find any memory effect that was distinguishable. As noted above, we also developed the CFLDI technique that innovated on the current state-of-the-art in terms of the optical arrangement used in order to access the boundary layer region over a flat plate interrogating the boundary layer to around 1.5mm off the flat plate surface. We used this diagnostic tool to make measurements of the hypersonic boundary layer and noted that in these un-heated model tests, a second-mode frequency around 300 kHz was observable. We utilized the CFLDI set-up to test the cold model to confirm if the CFLDI measurements also showed a lack of the memory effect in the flowfield when boundary layer trips are utilized. This investigation used the flat plate instrumented with heat transfer and pressure sensors coupled with schlieren imaging and a cylindrically focused laser differential interferometry system to analyse the effects that boundary layer trips have on downstream boundary layer turbulence. A Mach 7.3 flow with an enthalpy of 1.5 MJ/kg was used to analyse various boundary layer trips with k/δ ratios of 1.9, 2.7 and 4.0. Analysis of the schlieren images showed an increase in boundary layer height of approximately 50% when a boundary layer trip was introduced into the flow. The disturbance spectra obtained from the cylindrically focused laser differential interferometry showed the shape of the spectrum to match well between the untripped and tripped cases. The magnitude of the fluctuations decreased when boundary layer trips were used, however the magnitude of the fluctuations did not change when the trip height was increased.

In year 3, we conducted testing with the heated plate along with CFLDI. These measurements were conducted a bit more upstream of the previous measurements in year 2, as we had observed that previously we were mostly in the fully-turbulent region of the boundary layer. By moving the probe location upstream we hoped to also measure some of the second mode frequencies. The mea-

surements demonstrated that the unheated model had a distinctive second-mode frequency of around 300kHz. With heating the model (up to a maximum temperature of around 800K) we observed a break down of the flow into turbulence. In some cases, we could observe what looked like a suppression of both the frequency (down to about 100kHz) and the amplitude of the disturbances within the boundary layer. This is consistent with the linear stability theory. However, what is inconsistent was the fact that the flow was still transitioning upstream of the unheated case. Similar, inconsistencies have also been observed in works by other groups that used a cooled model (cones) where the transition was delayed. At the recent portfolio review, we got in contact with a few groups that are interested in undertaking a stability analysis of our experiment to examine why the boundary layer transitions earlier. We hope to pursue these collaborations along with further analysis of our data obtained just before the project concluded in the coming months and report them in peer-reviewed archival publications.

Contents

List of Figures

List of Tables

1

Introduction & Background

Hypersonic vehicles travelling in the Earth's atmosphere experience large amounts of wall heating due to viscous forces acting within the boundary layer. The boundary layer is key in understanding aerodynamic drag forces and heating a vehicle will experience during flight. Hirschel's review article [2] notes that the hot surface of a vehicle will affect important aerothermodynamic properties such as viscous drag, heat loads, and other boundary layer properties such as turbulence levels. Heated boundary layers experience the following changes compared to cold boundary layers: *higher sonic line, increased viscosity close to the wall, altered baroclinic term (the lower density at the wall will respond differently to pressure gradients) and a larger boundary layer height*. Elevated wall temperatures from aerodynamic heating increase the near-wall viscosity and decrease density. A thicker boundary layer forms due to a decrease in flow momentum dissipation effciency and energy transfer. The thickening of the boundary layer also moves up the sonic line away from the wall, which will directly affect the region where the trapped acoustic instabilities propagate [3]. These changes affect important phenomena, such as turbulence, which cannot be properly recreated over cold walls. Investigating the growth of turbulence is important as it is used to predict the amount of aerodynamic heating and drag a vehicle will experience. Current experimental works undertaken in impulse facilities, such as shock tunnels, investigating the growth of turbulence typically only have cold walls owing to the low test times. As mentioned before, they do not accurately capture the boundary layer properties that would be experienced by a hypersonic vehicle in flight. These impulse facilities are however, good at producing high-enthalpy conditions akin to that experienced in true atmospheric flight under hypersonic conditions, but only for short test times. The result is that thermal equilibrium is not reached. A solution to this which has seen recent success is to heat the experimental models prior to the experimental run, such that more realistic wall-to-total-temperature ratio (T_w/T_0) ratios can be achieved.

The effect of high wall temperatures in hypersonic flow has not been extensively investigated in general. As mentioned eariler, it is known that increasing the wall temperature will increase the boundary layer thickness and decrease the skin friction and heat transfer to the wall. The research group in RWTH Aachen University [4–7] conducted a series of shock tunnel tests of preheated model to study the flow physics of hot-wall effects in scramjets. Recent numerical work on hot-wall effects in high-speed flows [8–11] mainly simulated the cases from supersonic flows to lower hypersonic flows ($2 < \mathrm{M} < 6$) with total flow temperatures less than 1200 K. One recent numerical investigation in a Mach 12 scramjet flowpath by our group showed that having the hot-walls modelled had important implications for the observed boundary layer thickness, internal shock reflections as well as combustion and extinction [12]. Thus, there is a need for further investigation of hot-wall effects in realistic high Mach number hypersonic flight conditions with a particular emphasis on obtaining qualitative and quantitative experimental data.

At the University of Queensland (UQ), the T4 reflected shock tunnel which is the proposed facility to undertake the current project, is specialized in generating Mach number, Reynolds number, and enthalpy matched "hypersonic flight" flow conditions. However, its millisecond order test time is insuf-

ficient to allow wall temperatures to reach the temperatures experienced in flight. Therefore, most of the previous works in T4 assumed isothermal walls with a temperature of 300 K [13–16]. Past experiments attempting heated models in T4 date more than a decade back and employed external heating (where an external heater radiates/conducts heat to the test-model), and could only realise low wall temperatures. Recent experiments at The University of Queensland in the X2/X3 expansion tubes have shown good capability to produce model wall temperatures over 3000K using direct resistive-heating by passing high-amperage-currents in models made of graphite. This technique was employed typically over small-sized models in the X2 expansion tube. Such experiments have not yet been carried out in the T4 reflected shock tunnel, where the test section is much larger and hence much larger models can be employed.

Hypersonic boundary layer transition is a difficult topic that has been investigated for years and is known to be influenced by many parameters [17]. Previously, both natural and forced hypersonic boundary layer transition studies have been extensively conducted in high enthalpy, impulse facilities, such as the T4 shock tunnel, to study the physical properties of the turbulent boundary layers [18–20]. Transition is caused by instabilities initiated from disturbances external to the boundary layer that grow through various modes until breaking down into turbulence [21]. The discrepancy between ground test facilities and flight conditions coupled with transition's many parameters make it challenging to predict and model without large amounts of uncertainty [22].

One parameter of particular interest is surface roughness. The effect surface roughness has on transition can be exploited, through the use of isolated roughness elements known as boundary layer trips, to force transition at a location allowing for the state of the boundary layer to be known. Boundary layer trips can promote various mechanisms for transition but the most effective disturbance is a streamwise vortex which travels downstream [23, 24]. Boundary layer trips are designed to introduce streamwise vortices into the laminar boundary layer while minimising drag and unnatural flow characteristics [25].

Boundary layer trips have two main practical applications. The first is to promote transition at desired locations on hypersonic vehicles where laminar boundary layers are not wanted due to separation concerns. The second is for ground facility testing of turbulence which are size constrained and cannot afford to have a model big enough for natural transition to occur. For both of these applications it is important to understand the downstream effects of boundary layer trips and whether the turbulent boundary layer produced is representative of a naturally transitioned flow and if not, what are the differences. A number of investigators have studied the impacts of trip size and shape on the transition location. These investigations have used a variety of different measurement techniques such as oil flow, heat transfer gauges, azobenzene surface sublimation, phosphor thermography and schlieren imaging [25–28]. However, a large number of these investigations focus on the effect that boundary layer trips have on the transition location rather than the downstream flow field within the turbulent boundary layer. This investigation will focus on the analysis of the disturbance spectra present in the tripped and untripped boundary layers to gain an understanding of any key flow features that are present in a tripped boundary layer compared to one that has naturally transitioned.

Many of the above investigations were done however, with only cold models. And, the effect of wall temperature in hypersonic boundary layer transition and subsequent growth of turbulence was not captured. Low enthalpy facilities such as blow-down tunnels can match the wall temperature to stagnation temperatures of flight conditions (T_{wall}/T_0 ratio), however, they will not reproduce the true-flight flow conditions which shock tunnels can do. Therefore, for comparison against flight-enthalpy matched, albeit cold-model tests in shock tunnels and to match the T_{wall}/T_0 ratio similar to that of these cold-wall shock tunnel results, wall cooling was employed in low-enthalpy blow-down tunnels. Once this match was reasonable, the blow-down facilities operating without a cooled model could be thought to represent a flight equivalent experiment with the appropriate T_{wall}/T_0 ratio. According to Mack's classical boundary layer stability theory [29], cooling the surface will stabilize the first-mode instabilities but destabilizes the second-mode instabilities. In turn, the transition length is expected to increase in subsonic and low supersonic flows but decrease in hypersonic flows. A conflicting trend was found,

however, in experiments with hypersonic flow over a flat plate [17, 30], where cooling the wall in hypersonic flows increased transition length. Opposite trends from the cold-wall are expected in the hot-wall case, and the cone tests of Fedorov et al. [31] showed that the localized wall heating increased the second-mode and promoted faster transition. Considering that the wall temperature effect studies in hypersonic boundary layer transition were primarily done in conventional (low-enthalpy) hypersonic wind tunnels, there is a missing database of the numerical and experimental investigation of hot-wall flat plate models in impulse facilities with realistic (high-enthalpy) hypersonic flow conditions. In particular, it would be a more realistic comparison to flight conditions for a high-enthalpy tunnel experiment to have hot models than for a low-enthalpy facility to employ model wall-cooling to match high-enthalpy facilities without wall-heating and then varying the wall temperature to explore its effect. Therefore, the experimental work undertaken in this project aims to fill this gap and address the challenge of experimentally investigating the growth of turbulence in the boundary layer of a heated flat plate in the T4 shock tunnel at UQ by subjecting it to high-Mach number (>7) flows. These studies can pave the way to employ shock tunnels as an advanced ground testing method prior to flight tests.

In recent years there has been a large progression in optical systems used to diagnose turbulence within hypersonic boundary layers. High speed schlieren has been used to visualise and quantitatively measure the boundary layer instabilities present in hypersonic flows [32–34]. Improvements in photodiode sensing equipment and its detailed characterisation [35] has allowed for high frequency focused laser differential interferometry (FLDI) to measure turbulence and boundary layer instabilities in hypersonic flows both in the free-stream [36] and over simple models, such as over cone geometries [37–40]. Modifications to FLDI systems made by A Houpt [41], Houpt and Leonov [42] have allowed for similar measurements to be made over flat plate geometries. A recent investigation conducted by [43] used a multi-point cylindrically focused laser differential interferometer to take high frequency density gradient measurements within a tripped hypersonic flat plate boundary layer. Analysis of the turbulent spectrum showed an increase in energy for frequencies above 100 kHz. It is to be noted that the beam in this arrangement was focused to a vertical line, thus the fluctuations measured inside the boundary layer were averaged over the entire height of the boundary layer.

Year 1 of the project focused on creating this capability by carefully undertaking the work needed to engineer electrically heated hot models in the T4 facility. This included solving challenges with managing power requirements and determining the appropriate current/voltages to be applied; ensuring the thermal expansion of the model owing to heating did not result in warping or cracking when the model is clamped or fixed within the test section; and ensuring the heating/wall temperature condition could be quantified and was repeatable. This report documents how these various challenges were overcome. An additional concern when undertaking electrical heating is the safety of operation. In Year 1, this was also addressed via undertaking a critical design review of the capability developed by forming a committee of experienced T4 users (professors within the Centre for Hypersonics with decades of shock tunnel testing experience), electrical technicians, facility operators and technicians. This report also presents some sample results from the first test campaign with this newly developed capability that demonstrates the effect of the wall heating on the boundary layer thickness for two cases: a laminar test condition at Mach 7 enthalpy and a Mach 5.5 enthalpy case that was mostly turbulent in the experimental field-of-view (FOV). Schlieren imaging and IR thermography were employed in this first test campaign.

Year 2 of the project focused on first analysing the data from campaign 1 segregating the heated model tests which only had optical field-of-view measurements by means of schlieren imaging and IR surface thermography from the fully instrumented cold model tests that had surface pressure and heat transfer sensors. The data was collected over a broad range of unit Reynolds numbers, total enthalpy and total pressure conditions. These are presented in this report. The findings indicate that the boundary layer thickens appreciably for the heated model case, and the transition location moves upstream. For the cold model case, we were able to identify the transition zone using surface heat transfer data including features such as turbulent spots moving through the domain based on the temporal heat transfer

data. We spent the remainder of the year which had significant delays due to the impact of COVID-19 on developing the capability to employ an optical technique based on a modified version of Focused Laser Differential Interferometry (FLDI) that can integrate the temporal changes in density leading to an inference on the turbulence fluctuations at near wall locations (within the boundary layer). This technique was designed and assembled for bench-top testing where the results showed baseline confidence that the system can be used in an experimental campaign for further validation. We are presently setting up for a test campaign in our T4 shock tunnel that will utilise the FLDI technique to make measurements on the cold model, along with surface heat transfer measurements.

Year 3 of the project has focused thus far on developing the cylindrical focused laser differential interferometry optical technique for application over flat plates. This investigation aims to gain an understanding of the downstream effects of boundary layer trips on hypersonic flow (using a representative condition of Mach 7.3 and an enthalpy of 1.5 MJ/kg), and shed light on whether or not tripped turbulent boundary layers can be used as alternatives to naturally transitioned turbulent flows. This will be achieved by analysing the spectra of high frequency density fluctuations measured inside the boundary layer and comparing the results of various sized trips to a naturally transitioned boundary layer. In order to make these measurements, we have modified the optical path of an existing version of a cylindrical lens focused laser differential interferometry (CFLDI) technique [41, 42] by including a combination of axisymmetric and cylindrical optical components. This allows us to make high spatial resolution measurements within a thin hypersonic boundary layer over a flat plate without losing any of the laser beam due to obstruction from the model, while also improving the spatial resolution of the previous method. This work has been published in a recent invited article for *Experiments in Fluids* [44]. Finally, we also undertook the CFLDI measurements on the heated model investigating the effect of wall heating on transition and growth of boundary layer turbulence over a flat plate. The preliminary results of that campaign are also presented in this report. More detailed analysis is being completed and will be reported in future archival publications.

2

Experimental Approach

2.1 T4 Reflected Shock Tunnel

All experiments undertaken in this project will be conducted in The University of Queensland's free piston driven T4 Stalker tube. T4 is a reflected shock tunnel made up of a reservoir, piston, compression tube, shock tube, nozzle, test section and a dump tank. The reservoir is separated from the compression tube by a 90kg piston, the compression tube is separated from the shock tube by a steel diaphragm ranging from 1-6mm thick and the shock tube is separated from the nozzle, test section and dumb tank by a mylar diaphragm. Preparation to fire the tunnel is done by evacuating each section below 1 torr except the reservoir which is only vacuumed to around 40 kPa. The shock tube is filled with test gas, either dry air or nitrogen, to its desired pressure. The compression tube is filled with the driver gas which is either argon, helium or nitrogen and the reservoir is filled using compressed air. The firing process of the facility involves releasing the piston where it accelerates and travels down the compression tube compressing the driver gas until the steel diaphragm is ruptured. The rupturing of the diaphragm causes a shock to travel down the shock tube where it compresses the test gas. The driver gas is reflected at the end of the shock tube where the test gas is stagnated until the mylar diaphragm is ruptured. The test gas is then expanded through the nozzle and into the test section. A schematic of T4 is shown below in figure 2.1.

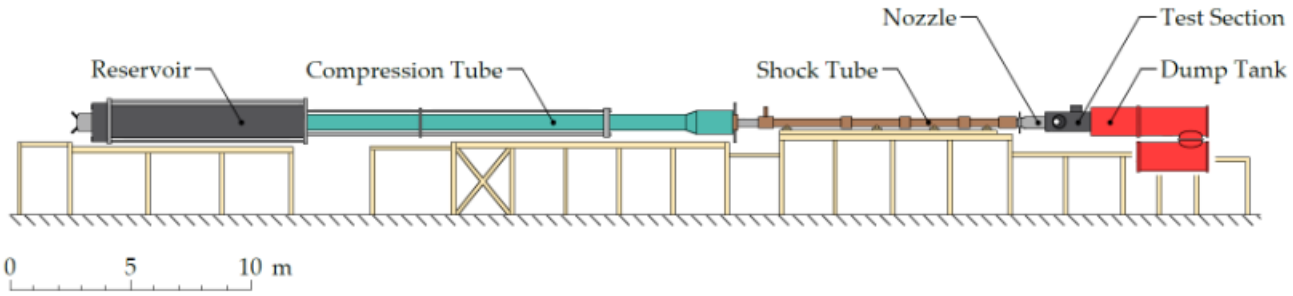

Figure 2.1: T4 schematic

The attractiveness of using a high-enthalpy test facility like T4 is that it provides flight matched test conditions. This is depicted in the T4 operability map in figure 2.2. The nominal freestream conditions used in our test campaigns for this project are presented in Table 2.1. All conditions were developed through an axisymmetric Mach 7 nozzle [45] of the University of Queensland's T4 free-piston driven shock tunnel [46]. The conditions aimed to produce Mach 7 flight enthalpy in 25 km altitude [47] (Mach 7A), Mach 8 flight enthalpy with higher temperature/velocity (Mach 8A), and Mach 5.5 flight enthalpy with different primary diaphragm thickness (Mach 5.5A and B) to generate higher density and Reynolds number. Freestream values were calculated using ESTCj [48].

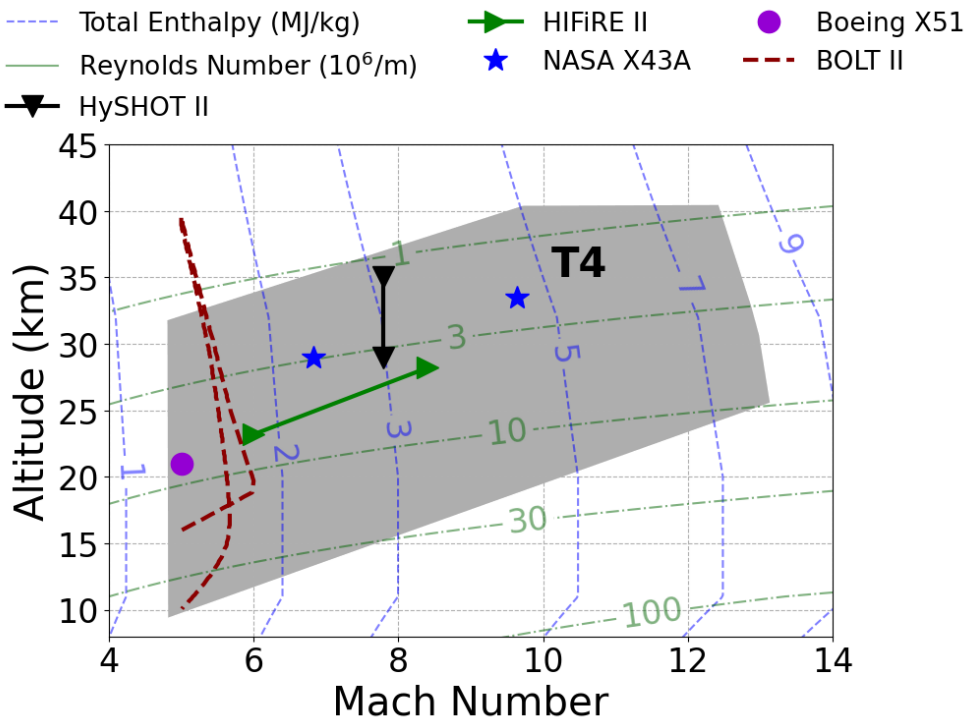

Figure 2.2: T4 flight-matched operability

Table 2.1: Nominal experimental freestream conditions.

Parameter	Mach 7A	Mach 8A	Mach 5.5A	Mach 5.5B
Pressure, p_∞ (Pa)	2550	2138	2557	3531
Temperature, T_∞ (K)	252	305	163	153
Velocity, u_∞ (m·s^{-1})	2226	2398	1861	1813
Enthalpy, H_s (MJ·kg^{-1})	2.44	2.88	1.59	1.49
Mach number, M	7.00	6.85	7.27	7.30
Dynamic pressure, q_∞ (kPa)	60.8	70.3	94.7	131.9
Unit Reynolds number, $Re_\infty \times 10^6$ (m^{-1})	5.01	3.15	9.19	13.9

2.2 Heated Flat-Plate Model

The heated plate model has a metallic leading edge followed by a graphite flat section that is heated resistively by passing a high Amperage, direct current through it. The leading edge sharpness is an important parameter to ensure that the entropy layer is very small and does not interfere with the study of Mack mode instabilities and transition to turbulence. Hence, we sharpened the leading edge after manufacture and measured this sharpness and periodically re-sharpened it between shots. The graphite flat plate with its two rail-like legs is slotted into a copper electrode structure that clamps the plate legs. The design considerations included a requirement of the surface temperature of the plate to be able to reach values exceeding 1100 K. The following sections outline the design process and some of the challenges that were faced with the model.

2.2.1 Leading Edge

As noted earlier, the leading edge has to be maintained very sharp to avoid the entropy layer becoming significant. We manually sharpen our leading edge periodically to ensure it stays sharp throughout

our test campaign. The high-enthalpy shots in T4 will start to blunt this leading edge over a period of time, hence this procedure is performed to ensure we do not have a rounded leading edge as the campaign progresses. Figure 2.3 shows our measurement procedure, wherein, the leading edge is impressed upon a mould that is cured, sliced into pieces and then the leading edge sharpness is measured under a microscope. Our current estimate (at 100x magnification) is that the leading edge radius is around 8 microns.

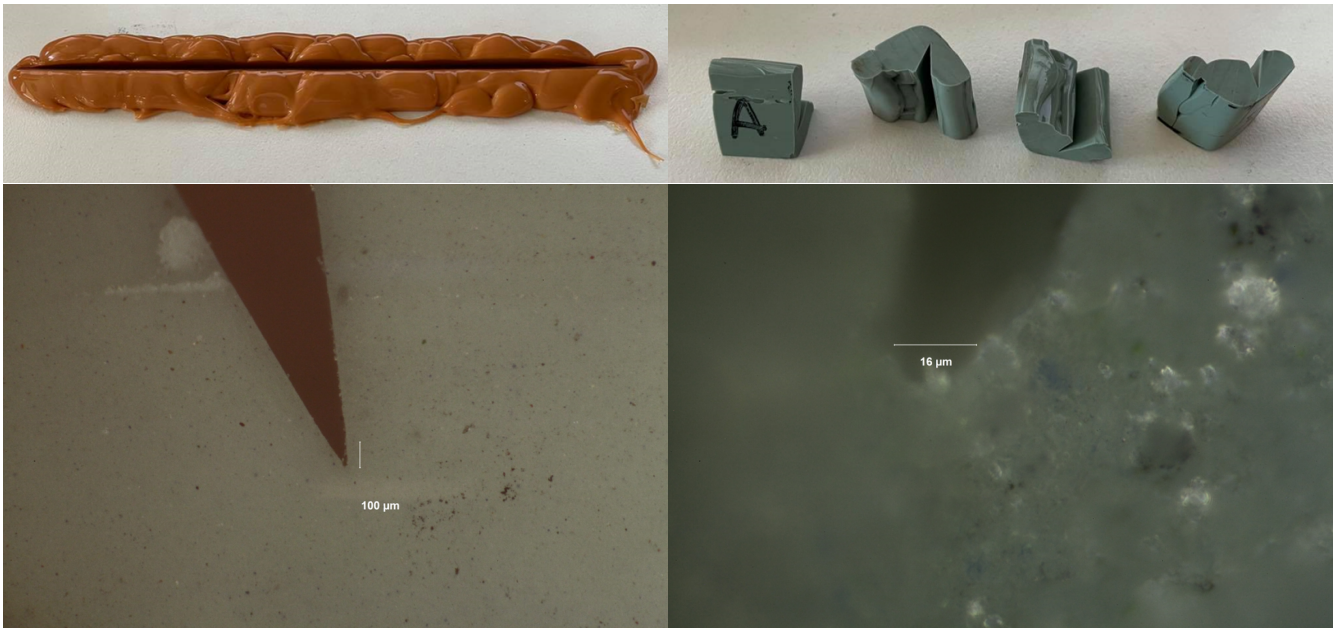

Figure 2.3: Leading Edge Sharpness Measurements

2.2.2 Plate Design

The project utilised two flat plate designs, a long plate and a short plate. Both plates were 100mm wide and 1mm thick with two legs 1mm thick. The short and long plates had lengths of 44.6mm and 81.4mm respectively. The CAD models and drawings are shown below.

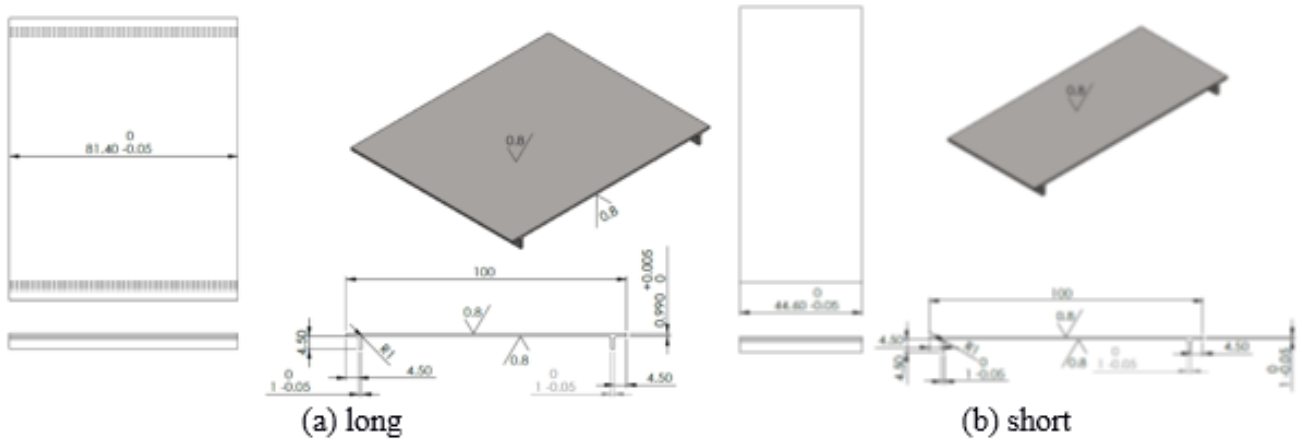

Figure 2.4: NUS invar36 heated plate designs

After the experimental campaign further bench-top testing was conducted to find the relationship between current supplied and surface temperature. After a few heating cycles it was found that the plate developed 'hot spots' on the heated surface. A hot spot is a region on the surface that has a higher sur-

face temperature usually formed by non-uniform contact between the plate and electrodes or a physical change in the surface such as oxidation. During the testing it was found that the plate could reach equilibrium temperatures of 1000k and 1100K using 600A and 750A respectively. These results gave a good baseline design for the plate needed in this experiment.

The initial design stages of the new plate required FEA validation to estimate and minimise the stresses and bending the plate would undergo when heated. An ANSYS simulation was set up of the NUS model to compare simulation results to the actual plate. Engineering material properties are fed into a thermal electric model as well as the applied current. The resulting surface temperature profile and plate constraints are inputted into a static structural model to gain the total deformation of the plate. This process is outlined in the flow chart below.

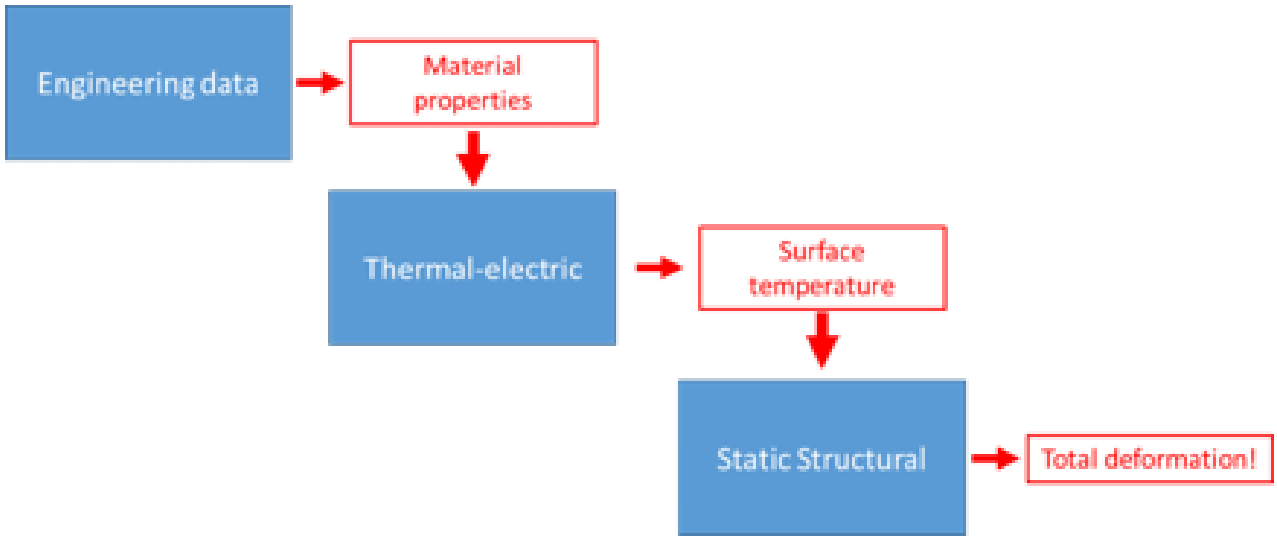

Figure 2.5: ANSYS FEA design validation process

The results of the FEA are verified by a visual comparison between the simulation and a plate which had been over constrained during a heating cycle. The results of this are shown below in figure 2.6.
Due to the nature of the investigation the new plate needed to be considerably longer so natural transition could occur within the length of the plate. The plate was made thicker to ensure it could withstand multiple heating cycles as well as hypersonic flow. The increase in material of the plate means higher amounts of power needs to be supplied to achieve similar temperatures as the NUS plate. When analysing equations 2.1 and 2.2 the increase in thickness and length both decrease the resistance and power dissipated over the plate.

$$R = \frac{\rho W}{tL} \tag{2.1}$$

Where W is the length the electricity has to travel, t and L are thickness and length of the plate respectively and make up the cross-sectional area the current travels through.

$$P = I^2 R \tag{2.2}$$

Where R is the resistance of the plate and I is the applied current.

To account for this resistance decrease due to plate dimensions the material was changed from invar36 to graphite due to the significantly higher resistivity. Figure 2.7 shows the cross-section of the new plate

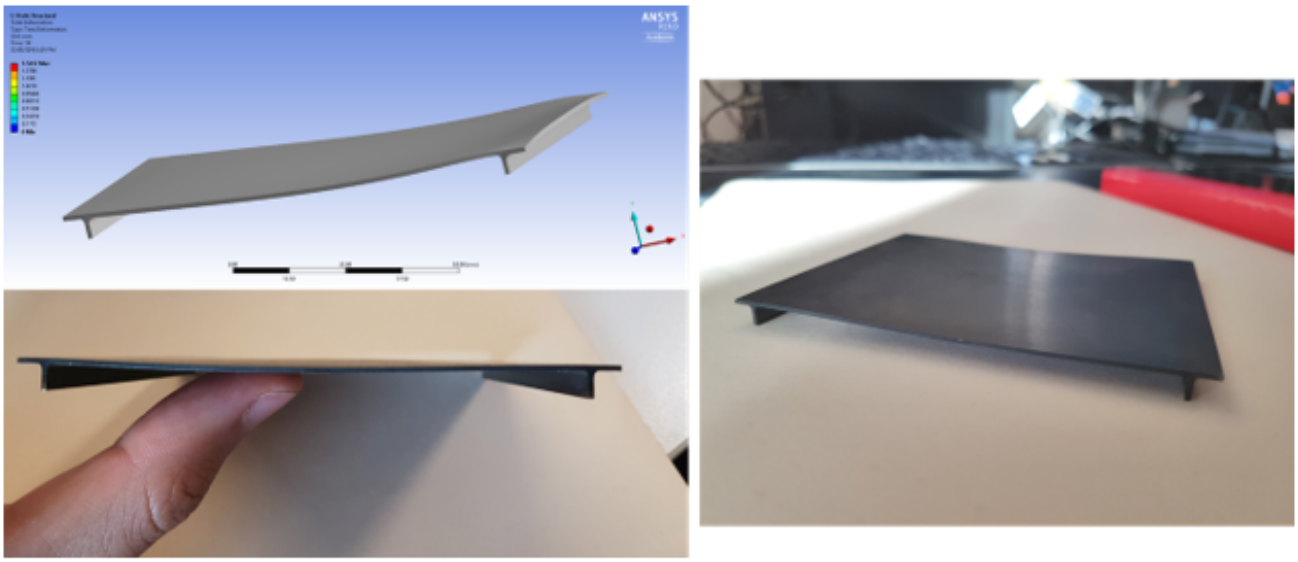

Figure 2.6: FEA validation results

that was simulated in FEA to find the method of constraining the plate which produces the least amount of deformation. The electrodes will be attached to the two 6mm thick legs and the plate has a length of 250mm.
Using the same process as figure 2.5 surface temperatures for currents in the range of 300A-900A were calculated and are shown in table 2.2.

Current (A)	Temperature (K)
300	515.5
400	589.9
500	655.2
600	713.8
700	768.6
800	832.2
900	874.6

Table 2.2: ANSYS predicted surface temperatures for applied currents

Using the maximum surface temperature of 874.6K four different plate leg constraints were tested to see which configuration produced the least amount of deformation. Figure 2.8 outlines the results of the simulations.
Figure 2.8(d) shows that having the legs free to move apart in the span-wise direction and able to expand perpendicular to the flow produces the least amount of deformation when heated up. This information is taken and applied to the design of the copper electrodes which are outlined in the next section of the report.

2.2.3 Support Structure Design

When designing the model there were four main facility related considerations that needed to be made: the nozzle core flow, flow blockage, nozzle movement and optical access.

Nozzle core flow: The useful cross-section of the core flow in an axisymmetric nozzle decreases due to expansion waves that form at the nozzle exit and propagate downstream. It was with this considera-

Figure 2.7: Cross-section of flat plate

tion that the model was to be placed in the nozzle so the boundary layer flow-field would be as close to 2D as possible.

Flow blockage: Models that are designed to sit inside of the nozzle create flow blockage. The cross-sectional area of the model must be designed so that it is small enough not to cause the nozzle to unstart slowing down the flow. Consideration around the angle of the model must also be taken into account as too large of an oblique shock can interact with the nozzle boundary layer further slowing down the flow. When the flow becomes too compressed on the underside of the model a large stagnation region can be formed which also stops the nozzle from starting up. Figure 2.9 shows the early design iterations to account for the flow blockage. The leading edge angle is decreased from 33 to 22.5 degrees, also to decrease the thickness (vertical distance) from 57 to 50mm at the same time.

Nozzle movement: Recoil in a shock facility causes the nozzle to move position within the test section. The facility initially recoils backwards as the piston is accelerated forwards. As the flow ruptures the diaphragms, it is expanded through the nozzle generating a thrust force which also pushes the facility backwards. Once the piston starts to slow down it starts to push the facility forwards. The shock absorbers are also helping to push the facility back into its initial position. However due to the mass of the facility and the momentum of the tunnel moving back into its initial position there is an overrun as the nozzle moves further forward into the test section. The position of the model mounting must be far enough into the tunnel that the overrun doesn't cause contact with the nozzle

Optical access: The current T4 schlieren visualization setup has a spherical mirror diameter of 200 mm. This means the maximum field-of-view is limited within 200 mm diameter circular beam, and the size of the flow-field that is intended to be observed must fit inside this.

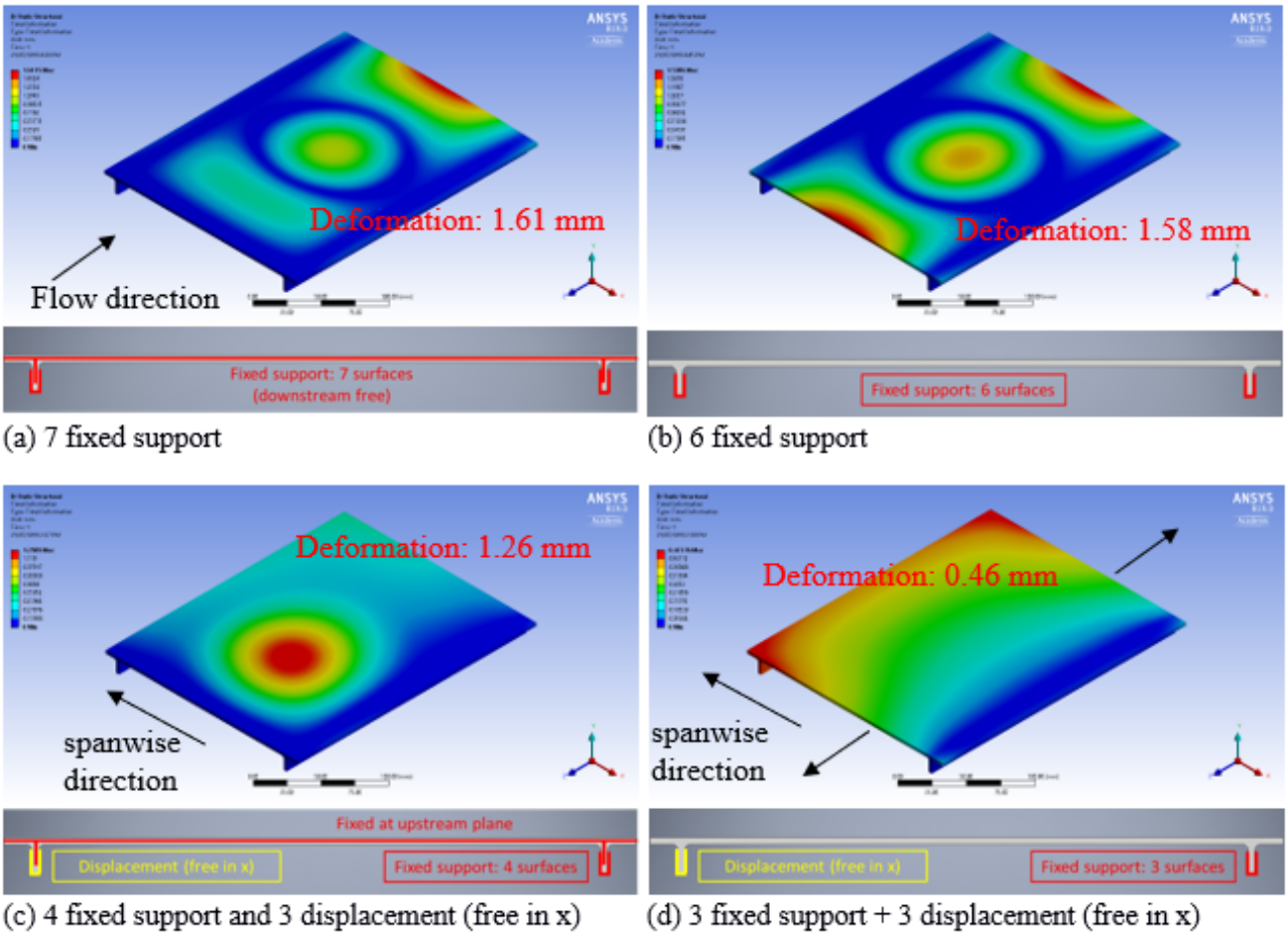

Figure 2.8: Flat plate deformation with various leg constraints

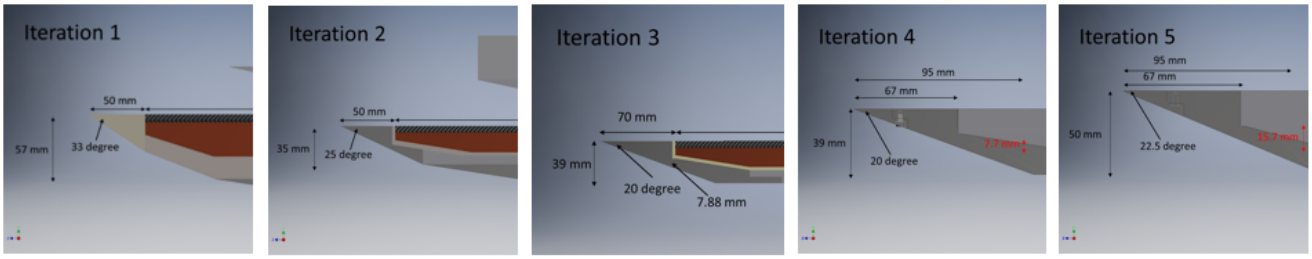

Figure 2.9: Design iterations to account for flow blockage

The support structure was made from steel to ensure it would be strong enough to resist any forces applied during tunnel shots. Since steel is electrically conductive it meant it could not come in contact with the copper else the current would pass through it due to it being the path of least resistance. Any surfaces that the copper must rest on the steel were covered in a high temperature non conductive ceramic, alumina.

2.2.4 Electrode Design

The electrodes were chose to be made from copper due to its low resistivity, high melting point and is manufacturable. A low resistivity means it can supply power to the model without dissipating too much

power and heating up. The high melting point is to ensure it is able to withstand high temperatures of the plate without jeopardising its structural integrity. Other important factors must be considered during the design of the electrodes and they are: the length, the width, heating, stiffness, clamping system and electrode securement to support structure.

Length: Sufficient streamwise length will allow boundary layer growth and natural transition to occur so turbulent flow can be observed.

Width: Sufficient spanwise width will ensure the test region is not disrupted by recirculating flow caused by the edge effect. It is also limited by the nozzle inner diameter.

Heating: The heated section must be able to reach the desired wall temperature from the direct-current power input. The heated section has a length of 250mm, a width of 200 mm, and a thickness of 3 mm.

Stiffness: The model structure must not experience any damage/destruction due to the flow after the test. The leading edge piece should be replaceable to account for damage due to diaphragm impact. As shown in figure 2.10, the current design employs a replaceable leading edge, with some modifications.

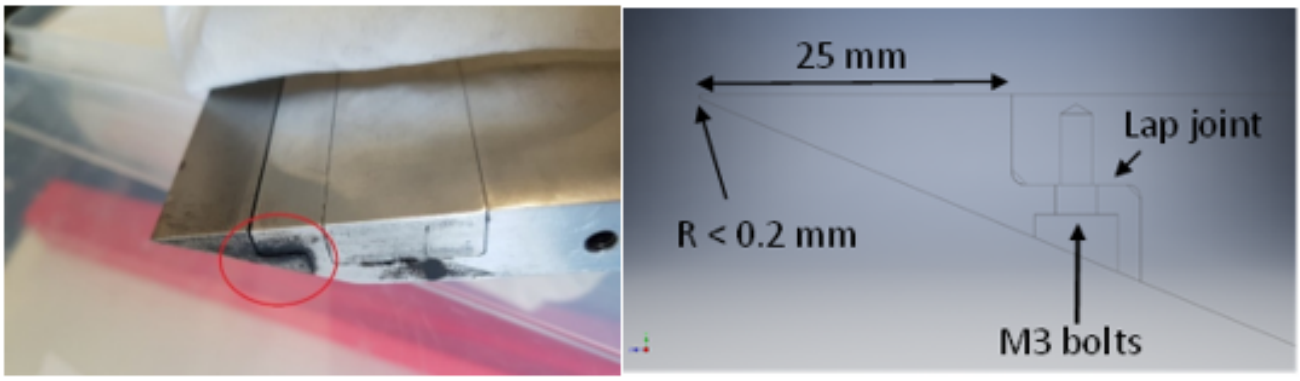

Figure 2.10: Existing leading edge (left) and current design (right)

Clamping system: A clamping system is used to attach the electrodes to the plate. The system utilises screws spaced 17.5mm apart to tighten and apply a uniform pressure along either side of the graphite legs. A uniform pressure is needed to ensure constant contact is maintained along the length of the plate. Without constant pressure local hots pots on the plate can form as well as increasing the contact resistance between the plate and the electrodes.Increased contact resistance increases the total system resistance (power supply, cables and model) which dictates the amount of power drawn from the wall. The maximum system resistance can be calculated by taking the lower of the power supply and wall power limits and rearranging equation 2.2 using the maximum current that will be supplied. The graphite plate, power supply and cable connections will all have fairly constant resistances, subtract those from the maximum system resistance to find the maximum contact resistance limit. The contact resistance is also affected by contaminants between the graphite plate and copper electrodes such as an oxidation layer. Copper shims (thin slit of copper) were found as a successful solution to reducing the contact resistance between plate and electrode. The copper shims were sanded with P1200 grade sandpaper to ensure no contaminants were present on the surface and were placed on the inside of each graphite leg. An exploded view of the clamping system can be seen below in figure 2.11.

Electrode securement to support structure: The electrodes and the support structure are not attached and reply on friction and physical blockages to stop the model from moving during the test time. As found in figure 2.8 (d) the plate legs need to be able to move freely relative to each other, hence the

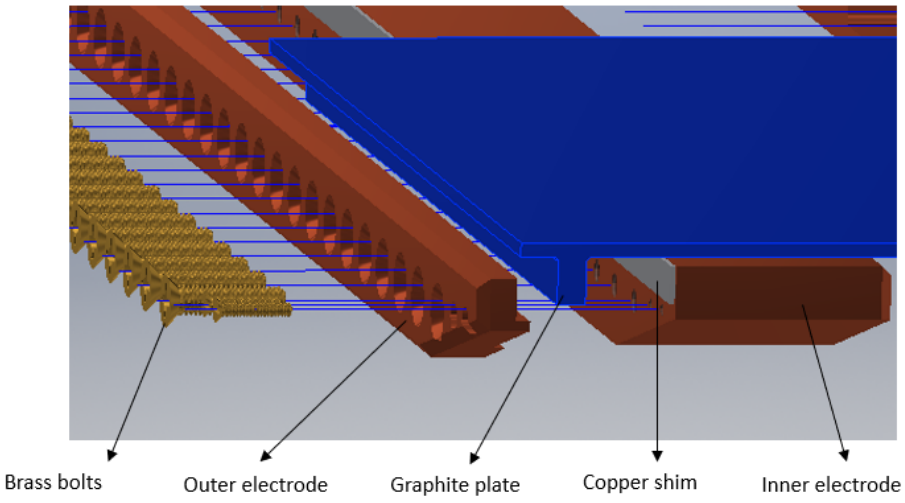

Figure 2.11: Electrode clamping system

copper electrodes are able to move freely in the spanwise direction. The FEA simulations also found that the legs need to be unconstrained in the streamwise direction which is not possible with the clamping system used. However copper has a thermal expansion coefficient three times that of graphite so when the plate is heated up it is able to expand in the streamwise direction with only a little amount of stress induced. The electrodes are held in place by opposing male and female parts to stop movement in the remaining two axis. The male and female parts of the electrodes and support structure are shown below in figure 2.12.

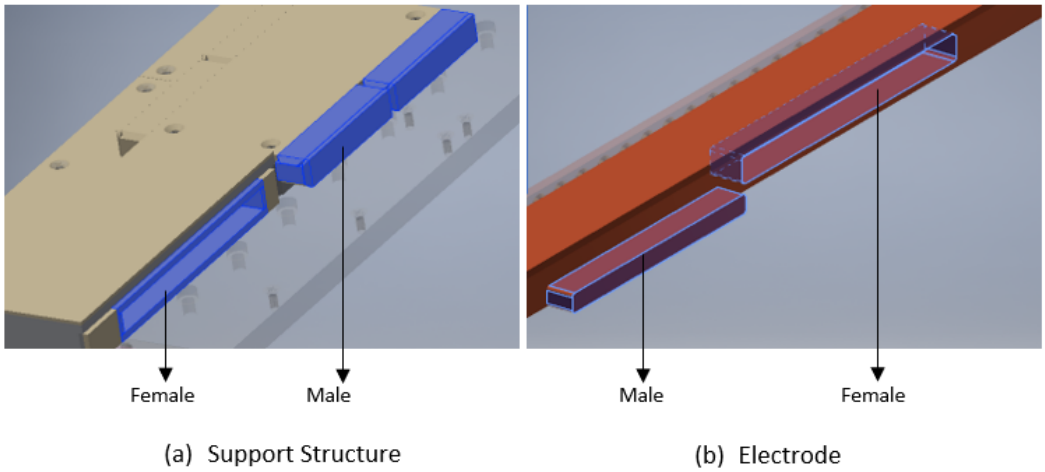

Figure 2.12: Electrode and support structure connections

The current design of the flat plate and support structure can be seen below in figures 2.13 and 2.14.

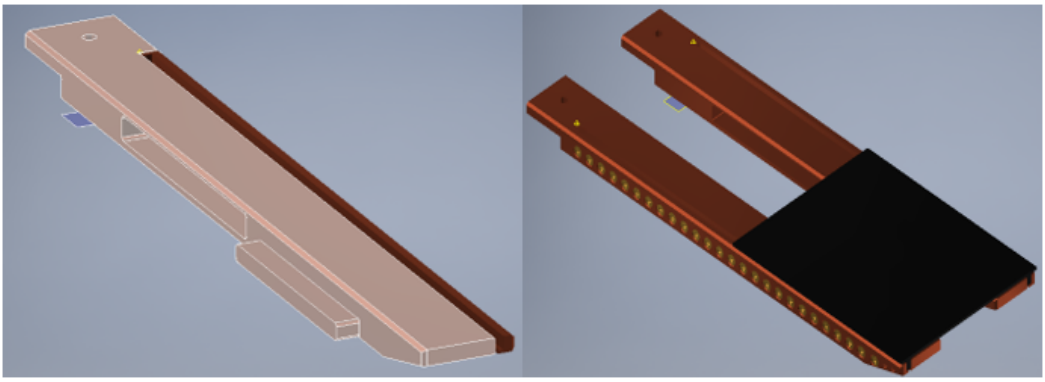

Figure 2.13: Electrodes and plate CAD

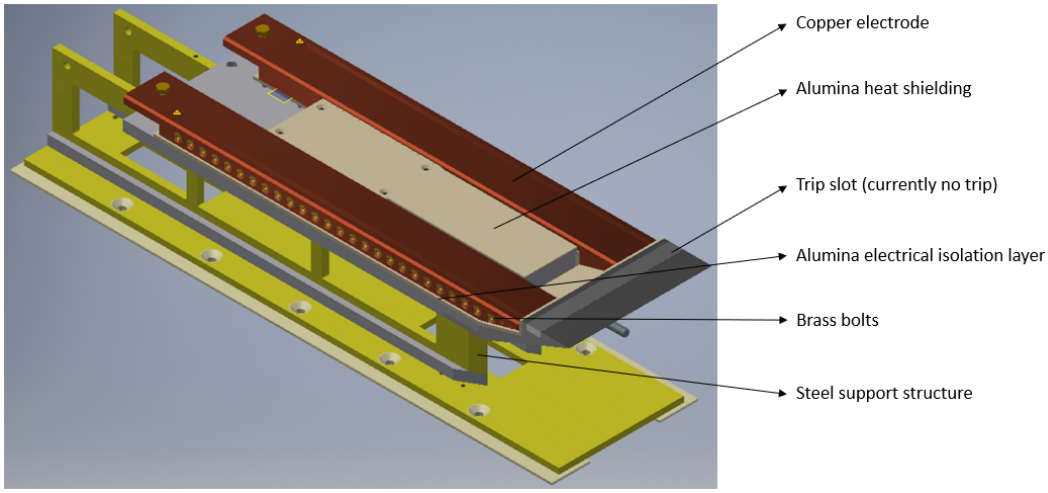

Figure 2.14: Electrode attached to support structure without plate

Bench Testing

Bench testing was conducted to find if the large graphite plate could be heated to high temperatures and the nature of the heat distribution along the plate. An infrared camera was placed above the plate as well as four thermocouples along the surface of the plate and one on the copper electrode. The setup of the bench testing is shown below in figure 2.15. Figure 2.15 also shows the plate successfully heating up to around 825K from a supply current of 1400A. This gave good confidence that the plate was to be heated to a high enough temperature in a reasonable amount of time. Figure 2.16 shows the results of the thermocouples for the successful heating cycle.

2.2.5 Vacuum Testing

Vacuum testing of the plate was conducted to find what surface temperatures could be achieve through different applied currents as well as cooling rates once the power is turned off. K-type thermocouples and an IR camera were used to calculate the surface temperature and visualise the temperature gradient along the face of the plate. The vacuum tests were conducted by applying a current to the model for 60 seconds and observing the surface temperature maximum surface temperature as well as the cooling of the model for 20 seconds after the power was switched off. Table 2.3 below shows the results of the testing.

The cooling rates of the plate are important as safety procedures require for the power to be switched off

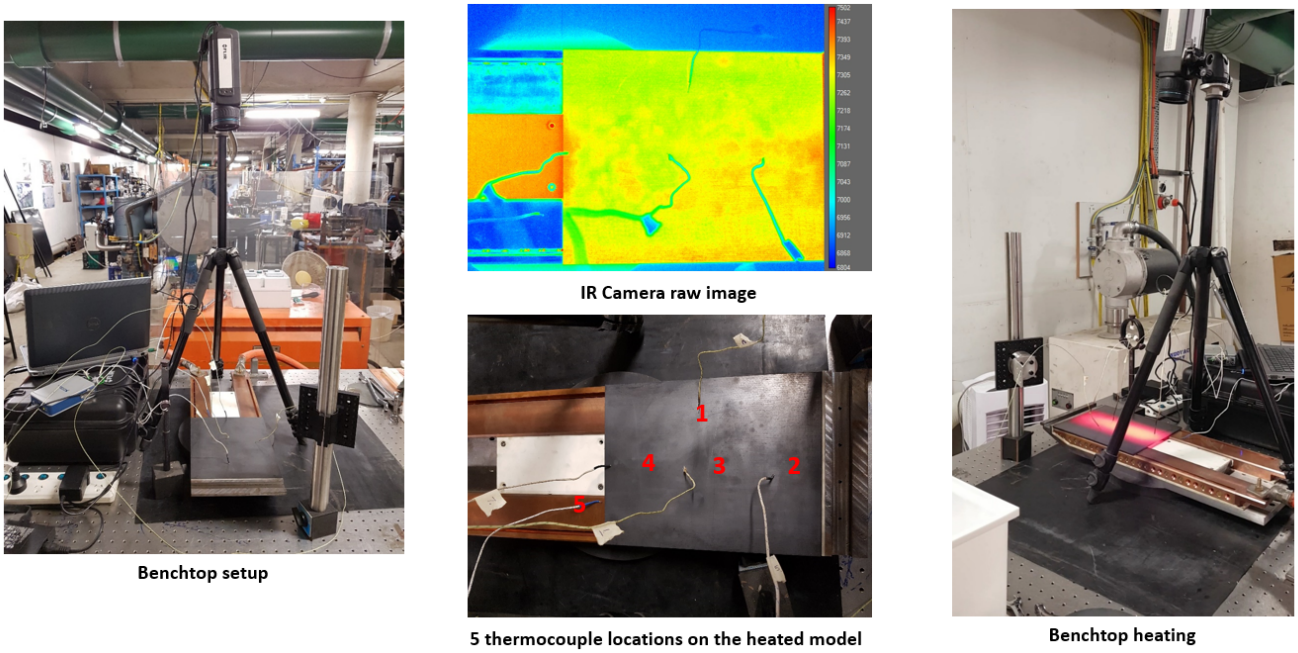

Figure 2.15: Bench testing setup and hot plate during a heating cycle

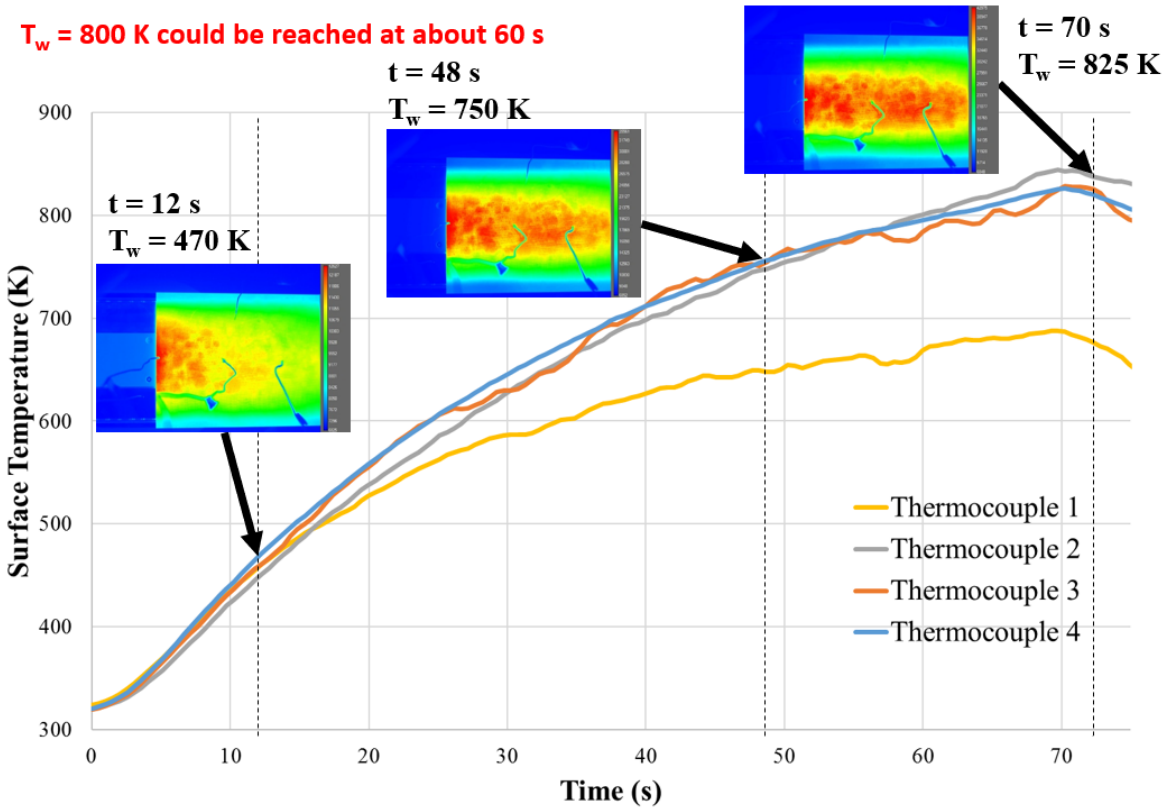

Figure 2.16: 1400A heating cycle thermocouple readings

before firing the tunnel and there generally is around a 10-20s delay between the two. Understanding the temperatures able to be reached after a specific time allow for easier coordination of the shot as all parties operating the tunnel know exactly when the power supply will be switched off and when it is safe to fire. Figures 2.17 and 2.18 below show the thermocouple and IR data for 1000A and 1500A vacuum tests.

Current (A)	Ts @ 60s (K)	Ts @ 80s (K)
300	343	334
500	393	371
700	509	495
1000	642	616
1200	715	682
1500	900	817

Table 2.3: Heated plate vacuum tests

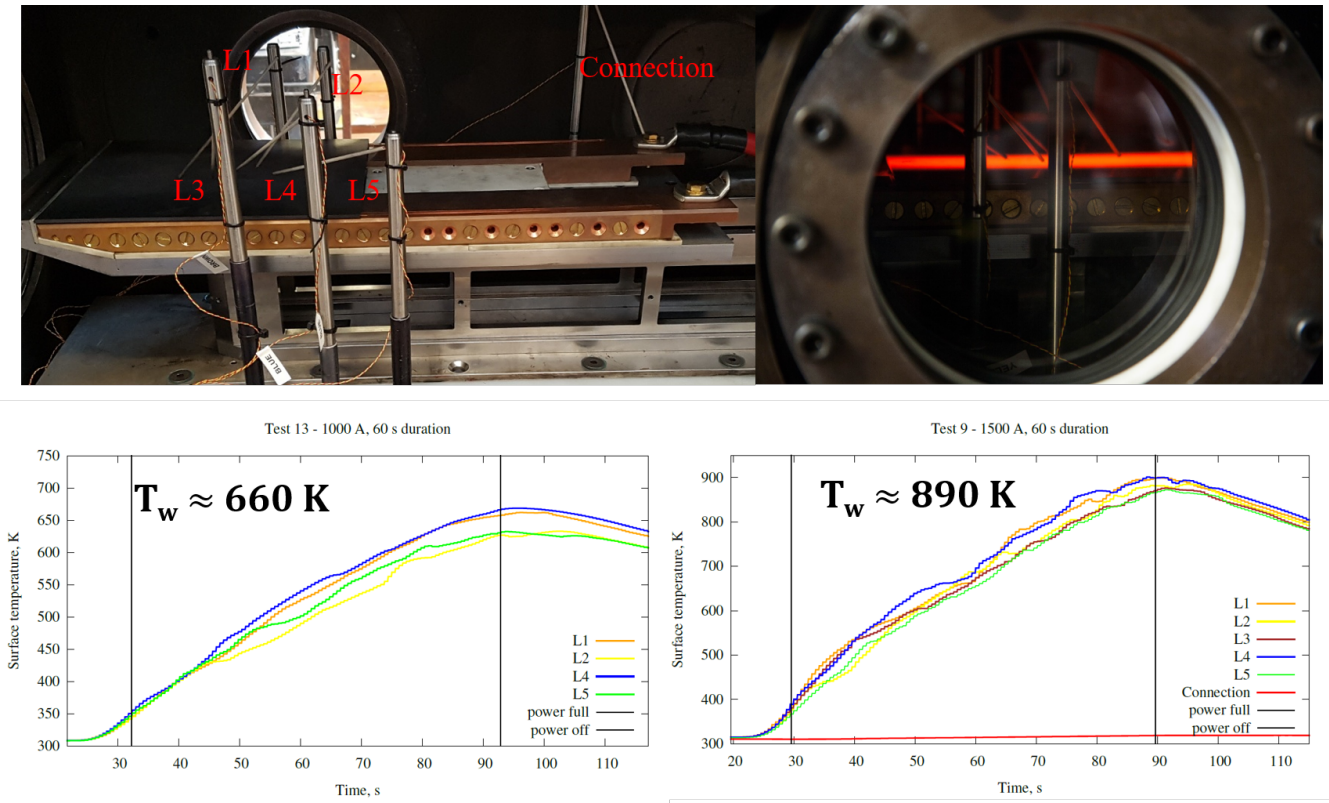

Figure 2.17: Vacuum tests in the T4 test section. Top-left: model with thermocouples, Top-right: Model glowing hot when heated, Bottom-left: Model subjected to 1000A of current for 60s and reaches ≈ 660K, and Bottom-right: Model subjected to 1500A of current for 60s and reaches ≈ 890K.

Using the thermocouple data and matching it to the IR images a calibration can be performed to read the correct temperature in the IF software, however this will be explained more in the next section. Analysis of the IR images can be done to produce two 1D temperature plots of the plate in the spanwise and streamwise direction. Due to the limitations of the size of the view window for the IR camera and the lenses viewing angle the entire plate is not able to be viewed while in the test section. The field of view that the IR camera can see is shown in figure 2.20.

2.2.6 IR Camera Calibration

Calibration of the IR camera was needed in order to accurately capture the temperature contour of the plate during the heating process and at the time of a shot. The calibration process involved two steps, first was to calibrate thermocouples and the second was to calibrate the IR camera. Five k type thermocouples were used for the calibrations. Each thermocouple was protected from high temperatures by a 150mm long ceramic sleeve and fibreglass insulator. The thermocouples were calibrated by a thermal well which could be set to specific temperatures. A calibrated thermometer was placed inside the ther-

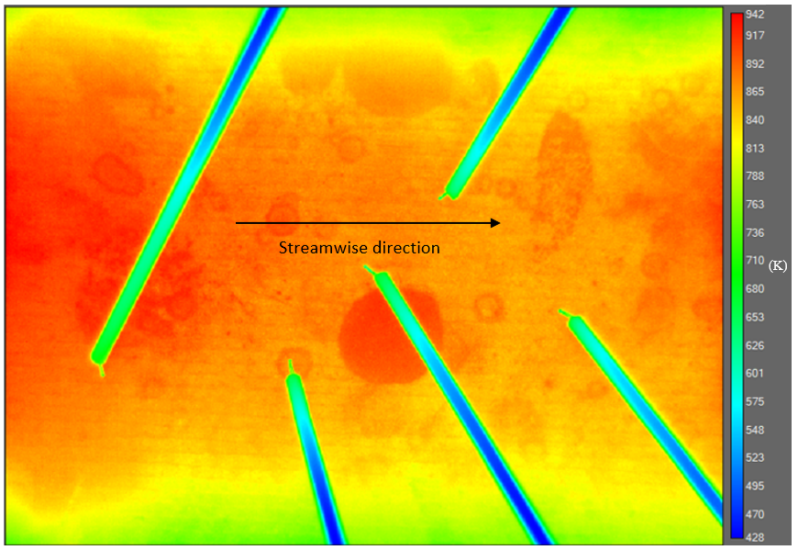

Figure 2.18: 1500A vacuum test IR camera data

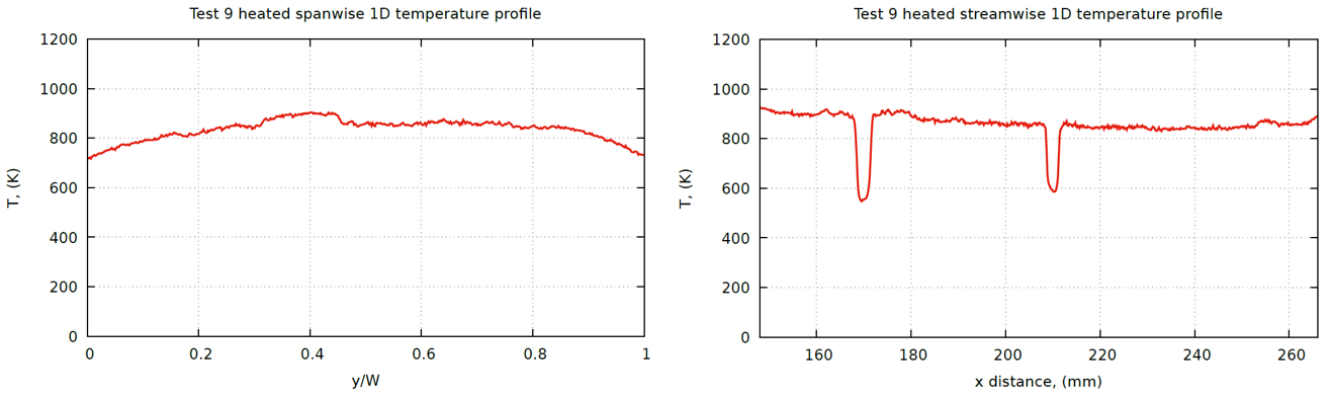

Figure 2.19: Spanwise and streamwise temperature profiles along the plate

mal well and was used as the known temperature to compare the thermocouple readings against. The thermal well was set to three different temperatures to get three data points for each thermocouple. A trend line was produced by performing a least squares analysis to produce linear equations between the thermocouple reading and the actual temperature. The thermocouples have been named using colours which co-inside with their wire insulation, the table below shows the results of the thermocouple calibration.

Using the data from table 2.5 the following linear equations can be formed for the thermocouples.

The second step of the calibration was to place thermocouples in the field of view of the IR camera and take the plate through a series of heating cycles while recording the IR images and thermocouple data. The IR images record the raw counts at a frequency of 25 Hz and the thermocouples record the temperature at 10 Hz. The two sets of data can be compared against each other by finding frames of the IR data that match the same time of the temperature data. The average of a 3x3 pixel square at the tip of the thermocouple in the IR image is plotted against the corresponding temperature recorded by the thermocouple. Similarly to the thermocouple calibration, the data is used to find an equation of best fit and this trend is used to post process all the IR images so the temperature contour within the field of view of the camera can be visualised. An example of an IR image being used to produce the calibration data is shown below in figure 2.21.

The IR camera needed to be toggled between two different exposure settings depending on the tempera-

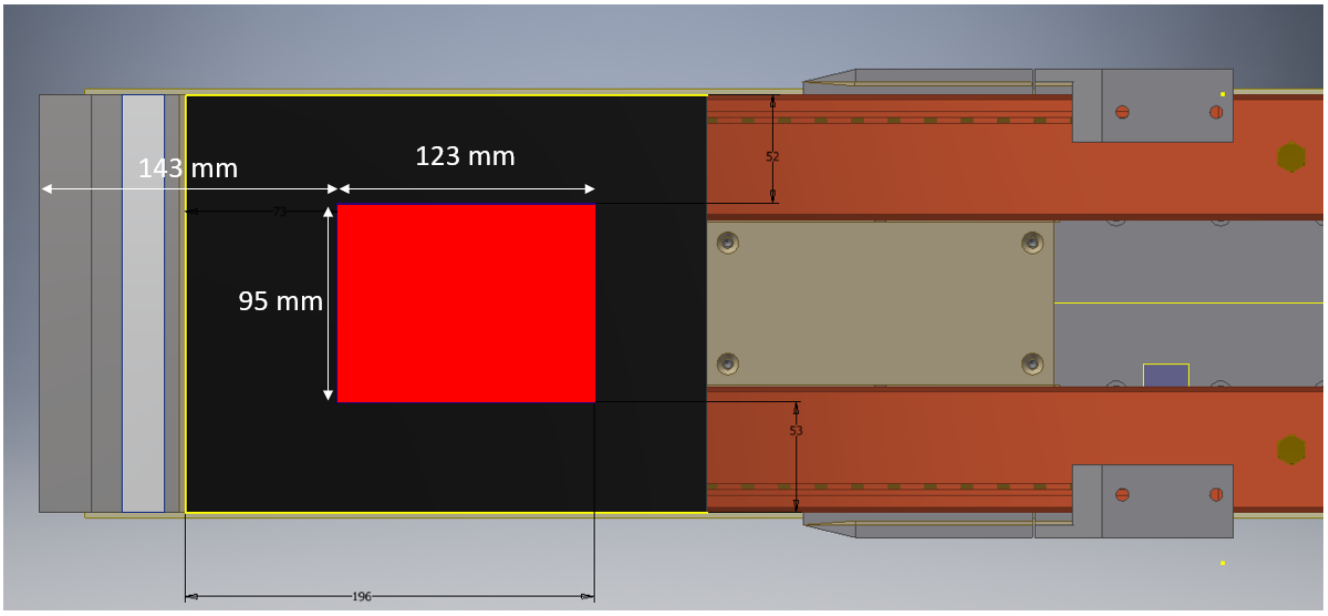

Figure 2.20: IR camera FOV of model in test section

		Temperature 1 (^oC)	Temperature 2 (^oC)	Temperature 3 (^oC)
Yellow	Well temperature	100.33	200.15	299.99
	Thermocouple temperature	99.86	198.92	298.339
Red	Well temperature	100.07	200.17	299.93
	Thermocouple temperature	99.20	197.65	296.45
Orange	Well temperature	100.07	200.17	299.93
	Thermocouple temperature	99.64	198.98	298.1
Green	Well temperature	100.08	200.15	300.01
	Thermocouple temperature	99.13	197.98	297.59
Brown	Well temperature	100.03	200.09	300.01
	Thermocouple temperature	99.4	198.16	297.82

Table 2.4: Thermocouple Calibration

Thermocouple	Equation
Yellow	$1.0059x - 0.0663$
Red	1.0132x-0.3198
Orange	1.0075x-0.3089
Green	1.0074x+0.3828
Brown	1.0079x+0.0217

Table 2.5: Thermocouple calibration equations

ture the plate was being heated to. The low exposure setting was used for temperatures up to around 600 K and the higher setting was used for anything above 600K. The need for this was because the camera would become over exposed and produce a saturated picture when using the low exposure setting for high temperatures but the higher exposure setting didn't show clear pictures of the plate around temperatures below 500K. The two different exposure settings both needed their own calibrations to be done.

When the tunnel is in the firing position the end of the nozzle comes into the FOV of the IR camera.

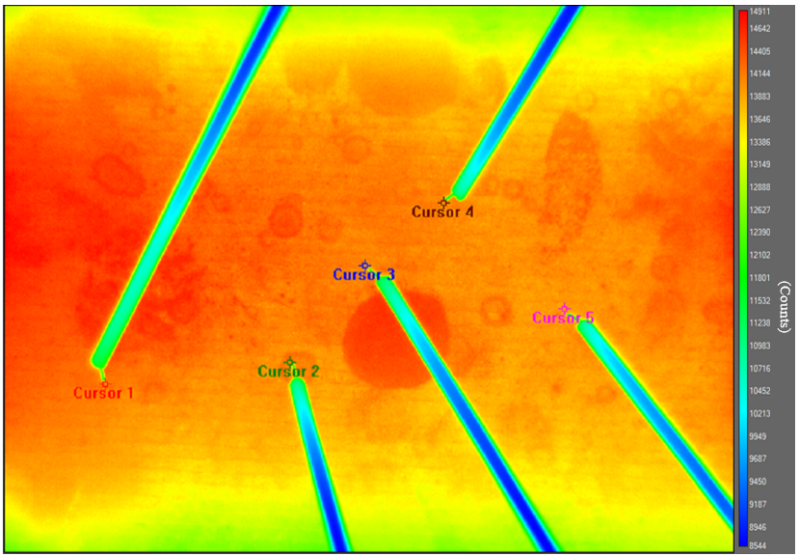

Figure 2.21: IR frame used for calibration

Due to the reflectiveness of the nozzle and the test section a superposition affect of the reflected infrared waves cause the camera to read higher counts than what the plate is actually emitting. As the tunnel fires the nozzle is pulled out of view of the IR camera due to recoil, thus eliminating all the reflective surfaces between the camera and the plate. This is known as the frame immediately after the nozzle recoil shows a large drop in counts. This effect meant that two configurations needed to be calibrated, one with the nozzle in the FOV so the temperature of the plate during the heating phase could be visualised and one without the nozzle in the FOV so the temperature of the plate during the shot could be calculated. A total of four calibrations needed to be conducted and each one took data from three identical tests to ensure they were consistent. The table below shows all the heating cycles done for the calibrations. An

Calibration	Heating Cycle	Layout	Description
1	1	Nozzle in FOV	Low exposure, 1000A for 60s
	2	Nozzle in FOV	Low exposure, 1000A for 60s
	3	Nozzle in FOV	Low exposure, 1000A for 60s
2	1	Nozzle in FOV	High exposure, 1500A for 90s
	2	Nozzle in FOV	High exposure, 1500A for 90s
	3	Nozzle in FOV	High exposure, 1500A for 90s
3	1	Nozzle out of FOV	Low exposure, 1000A for 60s
	2	Nozzle out of FOV	Low exposure, 1000A for 60s
	3	Nozzle out of FOV	Low exposure, 1000A for 60s
4	1	Nozzle out of FOV	High exposure, 1500A for 90s
	2	Nozzle out of FOV	High exposure, 1500A for 90s
	3	Nozzle out of FOV	High exposure, 1500A for 90s

Table 2.6: Calibration test matrix

example of an IR calibration is shown below in figure 2.22.

2.3 Cold Instrumented Flat-Plate Model

Figure 2.23 illustrates the instrumented flat plate experimental model. This "cold" flat plate was also commenced with a sharp replaceable leading edge. The plate had the same spanwise width (200 mm) and the surface finish of the heated plate, yet a much longer streamwise length of 626 mm. On the plate's

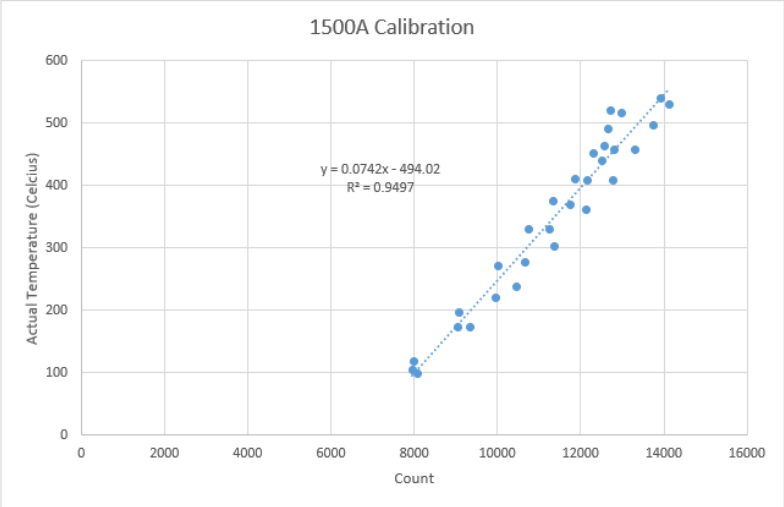

Figure 2.22: 1500A for 90 seconds test 1 calibration

surface, there were three arrays of instrumentations in streamwise direction to measure both pressure and heat transfer. Two 13 mm-spaced arrays with an offset of 6.5 mm distributed Kulite XTEL-190 (M) piezoresistive pressure transducers from 108 to 420 mm of the plate leading edge. Next to the Kulite arrays, thin-film heat transfer gauges (HTG) were spaced at 13.5 mm from 102 to 561 mm of the plate leading edge. Below the leading edge, a piezoelectric pressure probe in line with the flat plate was installed to measure the Pitot pressure of the nozzle core-flow. The 3D-printed shielding protected the sensor connections on the lower side of the plate.

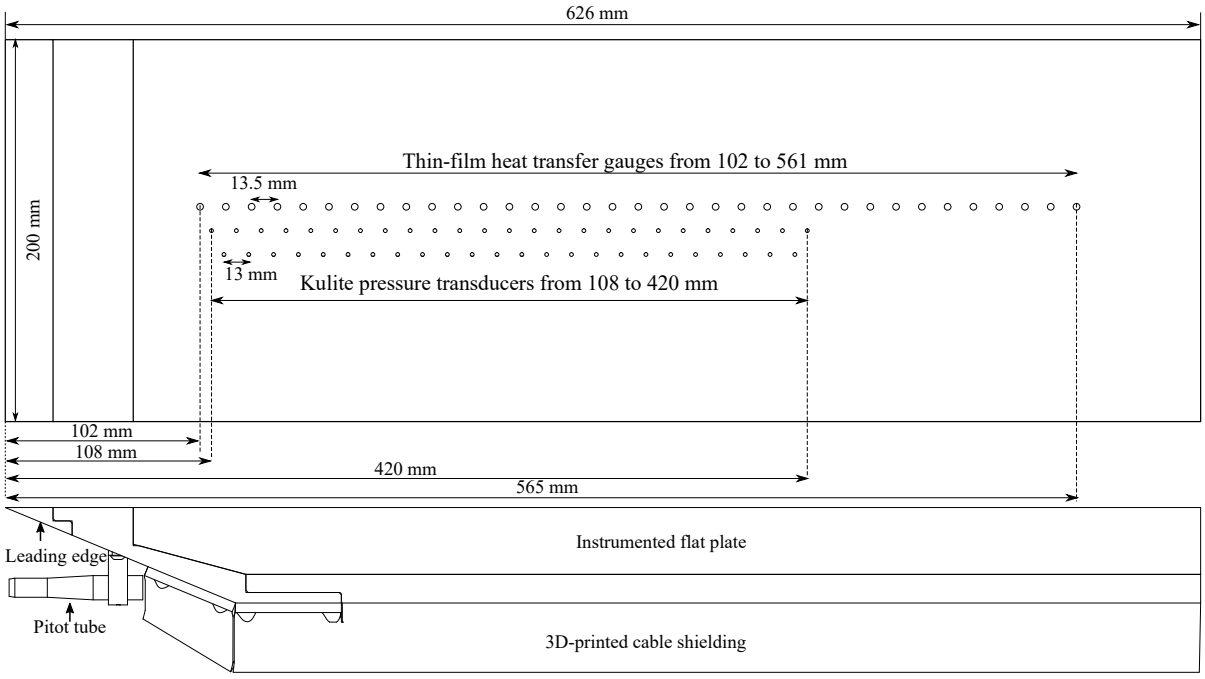

Figure 2.23: Schematic of the experimental model.

2.3.1 Thin Film Heat Transfer Gauges

Thin Film Heat Transfer Gauges (TFHTG) were designed and manufactured at The University of Queensland based on the process documented by Dann [1], and operating according to the semi-infinite fast

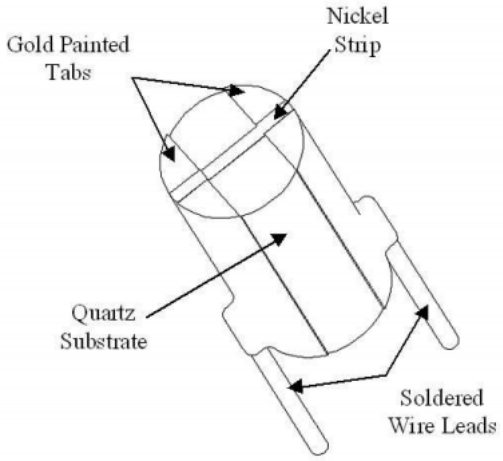

Figure 2.24: A Thin Film Heat Transfer Gauge [1]

response principle for impulse facilities developed by Schultz and Jones [49]. The gauges act as resistance thermometers to obtain temporal temperature measurements of the flow at the surface of the model with a response time of approximately 1μs. The time dependent temperature measurements are integrated to find the heat flux during the test time. The gauges (shown in Figure 2.24)consist of a polished quartz rod approximately 7–9 mm x 2 mm which are modelled as semi-infinite. A 1 mm x 3 mm x 0.1μm nickel strip is sputtered by an Edwards Auto 500 Sputtering machine connecting two gold tabs that run down each side of the rod. Copper wires soldered to the gold tabs run from the rods to circuit amplifiers and then to a data acquisition system sampling at 1 MHz. A 75μm layer of silicon dioxide is sputtered on the face to increase the gauge durability and to protect the nickel strip from any ionised particles caused by the flow [50].

The model was instrumented with 19 TFHTG located along the centreline of the model from 115–493.5 mm downstream of the leading edge. As the experimental campaign proceeded, the quality of the gauges degraded and some were rendered unusable by the end of the testing.

2.3.2 Pressure Sensors

Surface pressure measurements were acquired along the length of the flat plate through the use of 48 Kulite XTEL-190 (M) pressure transducers. The sensors were located from 108–498 mm in two streamwise rows, one positioned along the centreline and the other offset by 13mm as shown in Figure 2.23. The two rows were staggered so that the gauges had a downstream distance from each other of 6.5mm. The pressure transducers had ranges of 100, 175, 350 and 700 kPa, each with a measurement uncertainty of 0.5% of full scale output.

2.3.3 Surface Trips

To investigate the effect of forced-transition, we also attached a 1.4 mm-height boundary-layer trip [51] at 60 mm from the leading edge. This trip was manufactured/tested based on the NASA X-43A swept-ramp 2C design [25]. Regarding the present flow conditions, the trip achieved a trip-to-boundary layer height ratio $k/\delta \approx 1.7$ at 60 mm from the leading edge would be sufficient to trip the boundary layer as observed in previous T4 flat plate studies [51, 52].

2.4 Experimental Data Processing

The data acquisition system included 15 National Instruments PXI-6133 cards that produce analogue outputs of all channels at 1 MHz. The system was triggered by the piezoelectric pressure transducers detecting the flow arrival in the nozzle-supply. The Kulite pressure transducers measured absolute pres-

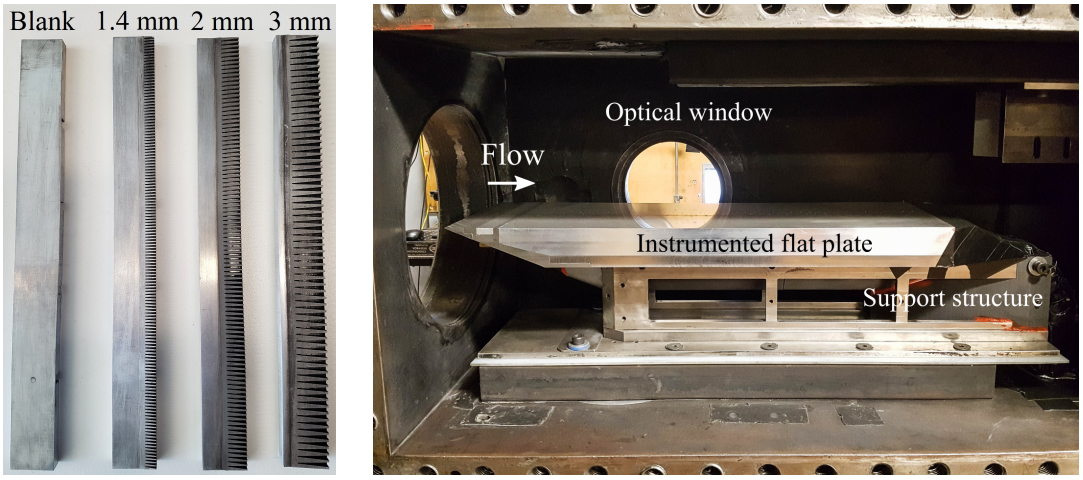

Figure 2.25: Swept-ramp boundary layer trip (left) and the experimental model in the test section (right).

sures, and flush-mounted HTGs measured wall heat transfer. HTGs used thin ($\approx$ 20 nm) nickel film, which was sputtered upon a quartz substrate to measure the voltage drop (change in resistance due to temperature) from hypersonic flow. The voltage drop was then converted into heat transfer ($\dot{q}$) using the deconvolution process outlined in [53].

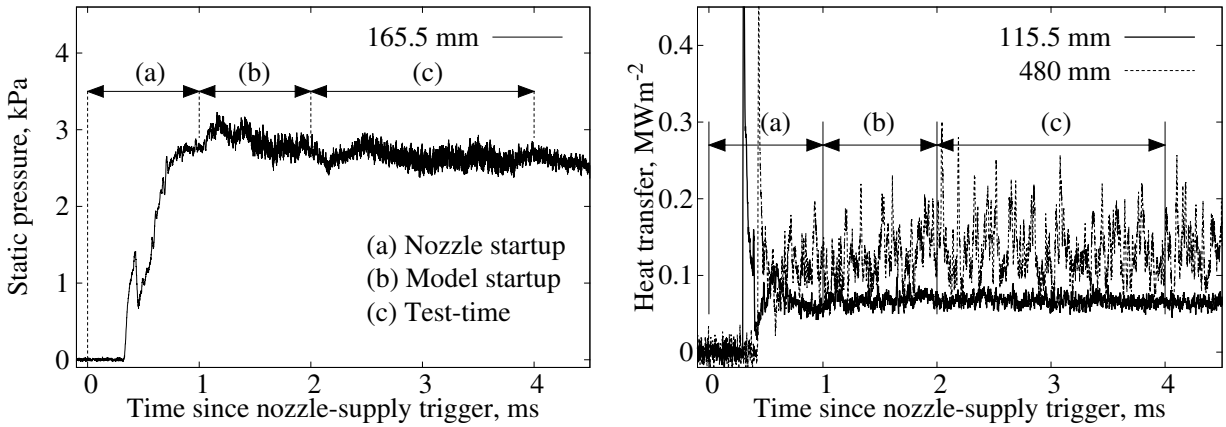

Figure 2.26: Typical static pressure and heat transfer traces from the experiment.

Fig. 2.26 shows typical traces from Kulite and HTG measurements during the experiment. The Mach 7 nozzle requires about 1 ms to start up, indicated by (a). After the nozzle starts up, the flow over the experimental model requires about 1 ms to establish, labeled in (b). (b) is measured to be slightly more than three flow lengths [54] of the experimental model. When the flow is established, the test-time begins and the mean value is taken during (c). During the test-time, both pressure and heat transfer signals reach a steady level during the nozzle-supply duration. Fig. 2.26 also depicts two heat transfer signals for the same shot. The boundary layer at 115.5 mm is laminar. Then the boundary layer experiences transition, leading to a fully turbulent level at 480 mm. Here, we observe a higher magnitude of heat transfer and temporal fluctuations. After the test time of 4 ms, the nozzle-supply pressure decreases, and so do the wall pressure and heat transfer.

The averaged pressure and heat transfer values are normalized and presented in the Results chapter.The pressure is normalized by the first sensor pressure p_1 which measured 108 mm from the flat plate leading edge. The heat transfer is presented in the form of Stanton number. The Stanton number is calculated using averaged surface heat transfer ($\dot{q}$) from each gauge, freestream density (ρ_∞), velocity (u_∞),

nozzle-supply enthalpy (H_s), and enthalpy of air at T_w = 300 K (h_w):

$$St = \frac{\dot{q}}{\rho_\infty u_\infty (H_s - h_w)} \tag{2.3}$$

Using the derived freestream values in Table 2.1 and the uncertainties involved in manufacture and calibration, the uncertainties associated with normalized static pressure and Stanton number were estimated to be $\pm$ 2.5% and $\pm$ 16%, respectively.

3

Optical Measurements

3.1 Cylindrical Focused Laser Differential Interferometry

Focused laser differential interferometry (FLDI) allows for high speed non-intrusive density fluctuation measurements to be made on the order of tens of MHz. Its focusing nature allows for a probing volume with spatial resolution on the order of tens of millimetres in the spanwise direction and tens of micrometers in the streamwise direction. The technique is able to look past unwanted noise such as turbulent boundary layers present on test section windows and edge vortices formed by some models. FLDI has been successfully used to characterise freestream turbulence levels in hypersonic ground test facilities as well as detecting hypersonic boundary layer instabilities on cone models [37, 38, 55]. FLDI works by splitting a linearly polarised beam into two orthogonally polarised beams with a small divergence angle between them. The beams are then expanded and focused using spherical lenses to the region of interest, usually on the order of ten's of micrometers apart from each other. Away from the focal point, the two beams share a similar path so that the phase shift imparted by the refractive index of the gas is relatively constant. The spatial selectivity of the system occurs because the only region where the beams are separated is near the focal point and disturbances passing through this region make the largest contribution to the signal. The difference in phase is measured and used to calculate the density gradient between the beams at the focal point. FLDI is limited in its probing location by the shape of the beam profile. The beam must be totally unobstructed as it passes through the test section. This limits the height above a flat wall the system can measure to the radius of the beam at the model spanwise edge, which in some cases can be tens of millimetres. Figure 3.3 shows a FLDI beam profile intersecting with a flat plate geometry for near wall measurements. The expanding beam profile will appear worse than shown in the figure as it will be largely obstructed due to the intersection of the beam with the near and far sides of the model. A Houpt [41] were able to reduce this limitation and make flat plate boundary layer measurements by replacing the system's conventional spherical lenses with cylindrical lenses (CFLDI). The cylindrical lenses allowed for the beams to be focused in one dimension, specifically the direction parallel to the model surface. This created a beam profile that resembled a thin sheet rather than a cone. Figure 3.3 shows the CFLDI beam profile able to make near wall measurements. A Houpt [41] went on to compare measurements of the CFLDI with a standard FLDI set-up and the results showed good agreement between the two [42]. The drawback of the cylindrical lenses was that the beam profile focused to a vertical line with height equal to the beam thickness. This meant that the boundary layer measurements were being averaged over half of the boundary layer height as opposed to a point, capable of being achieved by the conventional spherical lenses.

A modified version of the CFLDI used by A Houpt [41] is used in this investigation. It uses a combination of spherical and cylindrical lenses to expand and focus the beam profiles in stages, allowing for the same thin sheet profile to be made while also focusing the beams to a point in the spanwise direction as seen in Figure 3.3. A schematic for the system is shown in Figure 3.1. The CFLDI beams were focused on the nozzle centreline 263 mm downstream from the model leading edge and 1.75 mm above the model surface. A 8 mW, 650 nm laser with beam diameter of 25 mm is passed through a 7 mm circular aper-

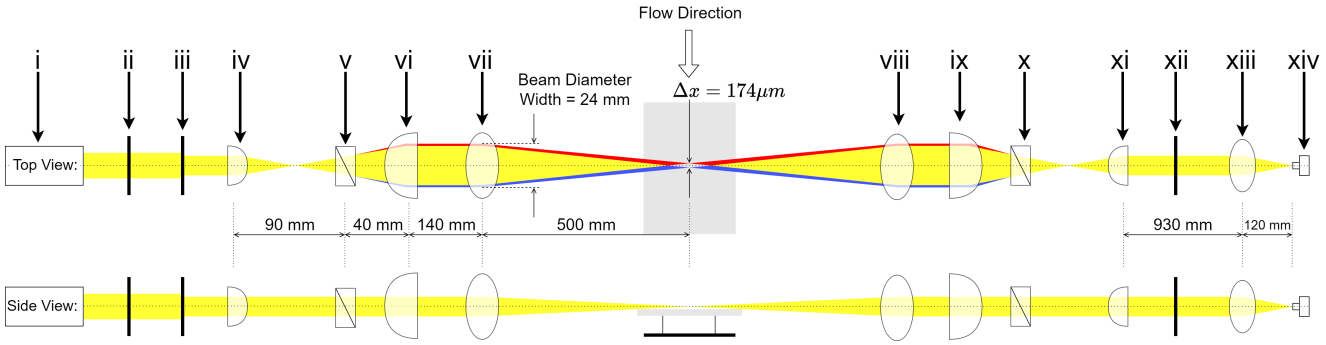

Figure 3.1: CFLDI system: i) Laser, ii) $45°$ Linear Polariser 1, iii) 7 mm Dia. Aperture, iv) Cylindrical Lens 1: f = 30 mm, v) Wollaston Prism 1: σ = 2′, vi) Cylindrical Lens 1: f = 100 mm, vii) Spherical Lens 1: f = 500 mm, viii) Spherical Lens 2: f = 500 mm, ix) Cylindrical Lens 2: f = 100 mm, x) Wollaston Prism 2: σ = 2′, xi) Cylindrical Lens 2: f = 30 mm, xii) $45°$ Linear Polariser 2, xiii) Spherical Lens: f = 100 mm, xiv) Photodetector

ture. The beam is then linearly polarised $45°$ relative to the plane of beam separation and expanded by a short focal length converging cylindrical lens in the direction parallel to the model surface. A Wollaston prism is used to the split the beam into two orthogonally polarised beams with a diverging angle of 2 arc minutes. The beams are then collimated by a cylindrical lens creating a thin sheet with a height of 7 mm and width of 24 mm. The collimated beam next passes through a spherical lens which focuses the thin sheets to two points with a finite separation, Δx. The beams are then reversed by a symmetric set of optics until passing through a spherical lens used to focus the beam onto the 3x3 mm sensor pad of the photodetector.

The beam separation at the focal point is found by analysing the ray diagram in Figure 3.2. Using trigonometry, an expression for the effective object height h at the diverging beam can be derived as follows:

$$h = 2w \tan\left(\frac{\sigma}{2}\right) \tag{3.1}$$

Where w is the distance between the prism and the object height and σ is the divergence angle imparted by the Wollaston prism. h' is an image of h with magnification M [56]:

$$h' = Mh \tag{3.2}$$

$$M = \frac{f2}{f1} = \frac{v}{u} \tag{3.3}$$

$$h' = \Delta x = \frac{2wv}{u} \tan\left(\frac{\sigma}{2}\right) \tag{3.4}$$

Where v is the distance between the image location and the focusing lens, u is the distance between the object location and collimating lens. The beam separation distance at the focal point, Δx, for the CFLDI system was 174$\pm$7 μm.
A $90°$ phase shift is imparted to the system before experimenting by shifting the second Wollaston prism in the plane perpendicular to the beam direction. As the prism is moved, the voltage response of the photodetector fluctuates between a maximum and minimum voltage corresponding to a $0°$ and $180°$ phase shift respectively. The prism is manoeuvred so that the average voltage rests half way between the two limiting voltages indicating a $90°$ phase shift has been imparted to the system [57]. A $90°$ phase shift is used, hence a linear relationship between voltage and phase change can be assumed [37].

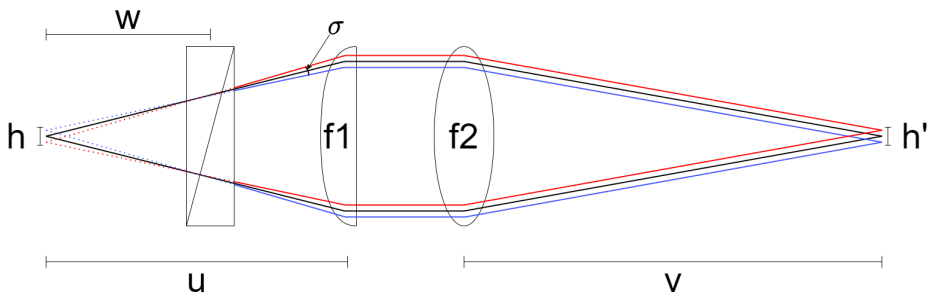

Figure 3.2: Beam separation due to the Wollaston prism.

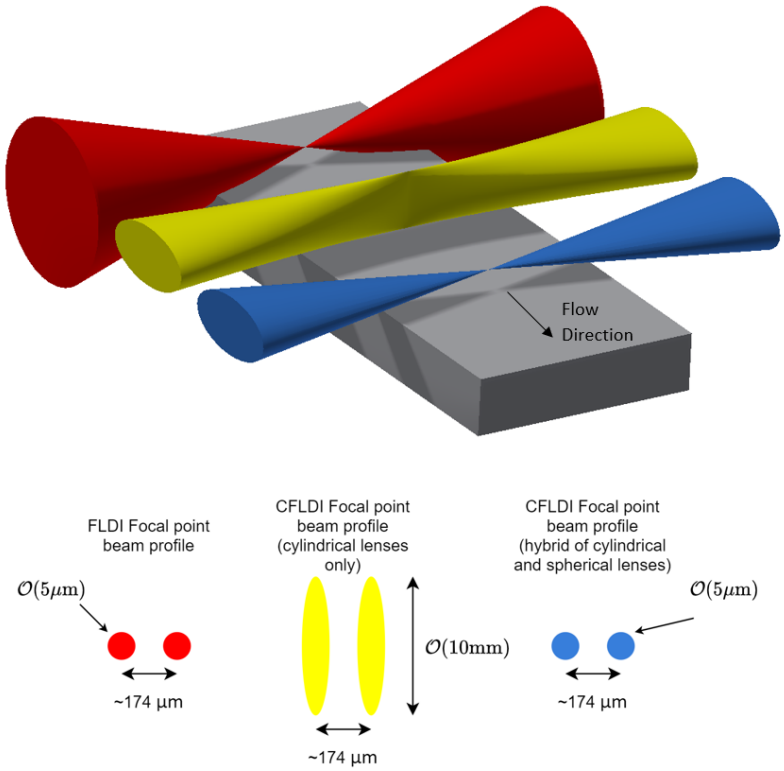

Figure 3.3: Beam profiles of FLDI and CFLDI systems, with the hybrid option of cylindrical & axisymmetric lenses developed in this study to interrogate the hypersonic boundary layer over a flat plate.

The measured voltage of the CFLDI system can be converted to a change in phase and density by the following equations derived by Parziale et al. [37].

$$\Delta\phi = \sin^{-1}\left(\frac{V}{V_0} - 1\right) \tag{3.5}$$

$$\Delta\rho = \frac{\lambda}{2\pi K L}\sin^{-1}\left(\frac{V}{V_0} - 1\right) \tag{3.6}$$

V_0 is the voltage of the system with a 90° phase shift, V is the output voltage of the photodetector, λ is the wavelength of the laser, K is the Gladstone-Dale constant for the gas ($2.248 \times 10^4\ m^3/kg$) and L is the integration length and is measured to be 48 mm by traversing a turbulent jet along the axis of the beam.

3.2 Schlieren Imaging

A Z-type schlieren set-up was used to visualise the hypersonic boundary layer. A green 15 A continuous LED was used as the light source which was reflected off a series of flat and spherical mirrors to produce a collimated beam through the test section which was eventually focused and captured by a high speed camera. The 190 mm diameter spherical mirrors had focal lengths of 2 m and bent the incoming and outgoing light by $8.4°$. The collimated beam length was approximately 5 m long. The high speed camera used was a Phantom v2012 which was sampled at 200 kHz with an exposure time of 0.48 μs and a resolution of 80x1280 px. The schlieren images were able to visualise from 175–335 mm downstream from the leading edge.

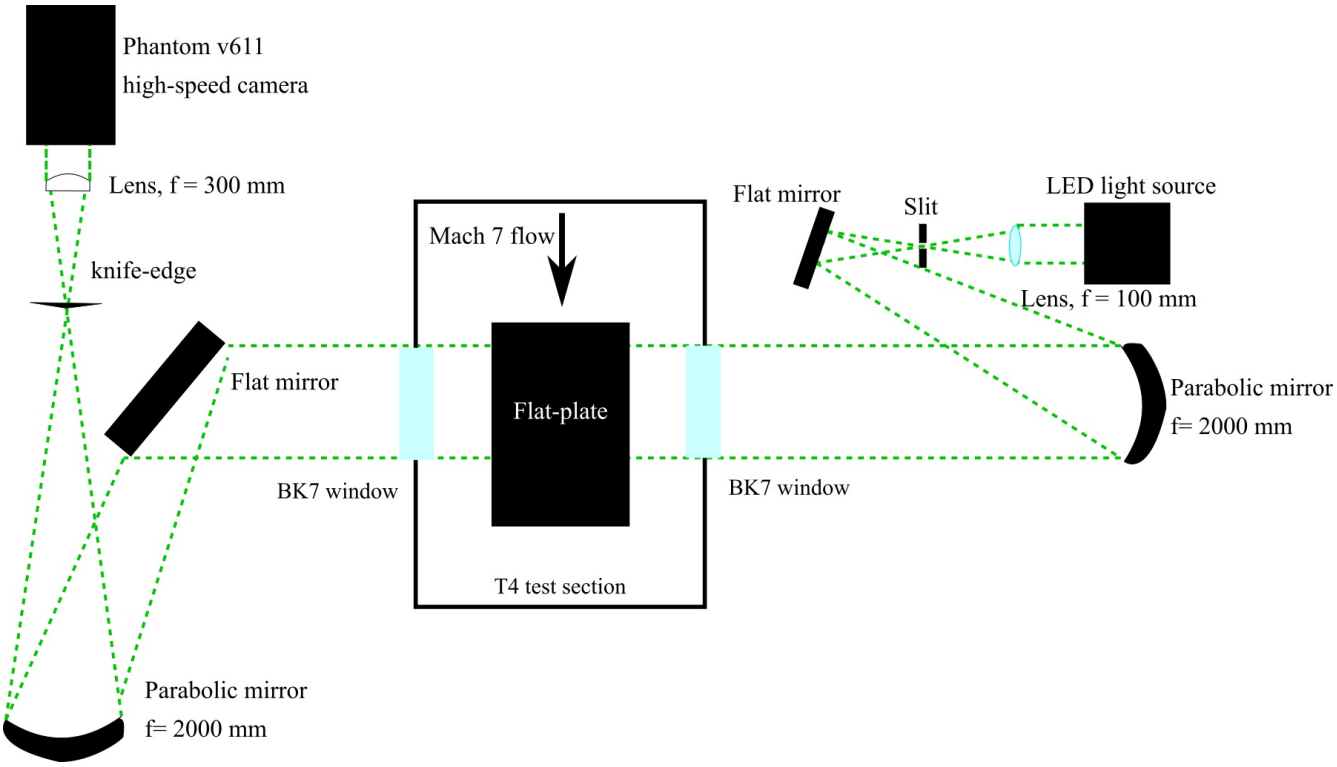

Figure 3.4: Z-type schlieren schematic.

4

Results

The results presented below are first for the test-campaigns with the unheated, instrumented model and then followed by the heated model results. The sequence of the results presented here does not follow the sequencing of the test campaigns. As indicated in the Abstract, we developed the heated model capability in Year 1 and demonstrated that in the first test campaign via schlieren imaging. Year 2 saw the development of the CFLDI optics that was deployed on the instrumented model in order to obtain comparisons with surface sensors vs boundary layer measurements using this technique. In Year 3, we used the CFLDI on the heated model to make measurements of the transitioning boundary layers. However, we decided it is best to present the results and "unheated" and "heated model" data as it logically separates out the effect of wall-temperature.

4.1 Unheated Model Results

4.1.1 Untripped Boundary Layer Results

To characterize the unheated boundary layers, we conducted shots with the instrumented flat plate to obtain the baseline surface pressure and heat-transfer. Figs. 4.1 to 4.4 show the surface properties of all the flow conditions. Flow direction is from left to right, and each plot includes a zoomed inset focusing on the schlieren field-of-view and temporal heat transfer plots at multiple locations. The theoretical Stanton number distribution as an output by the boundary layer program of Cebeci [52] is also plotted together for comparison. The heat transfer signals at 264 mm show that the boundary layer is laminar. Boundary layer transition is observed at 304.5 mm, where a turbulent spot is identified by a sharp increase in heat transfer toward the turbulent level. At the end of its passage, the values return to the laminar level. The heat transfer pattern agrees with our findings from the heated flat plate testing [47], where unstable boundary layer structures were observed at the end of the schlieren field-of-view. The boundary becomes fully turbulent by 439.5 mm, where both the heat transfer level and the magnitude of the fluctuation are significantly higher than those of the laminar boundary layer. The Reynolds number at this location is 2.16×10^6, consistent with the transition Reynolds number of $\approx 2 \times 10^6$ developed from previous flat plate studies in T4 [19].

For the Mach 8A condition, Fig. 4.2 indicates that a lower Re_∞ (3.15×10^6 m^{-1}) causes the transition to occur further downstream. Compared with the experimental Stanton number distribution, the boundary layer patterns in the schlieren image displays that the boundary layer stays laminar throughout. The turbulent spot is only captured at 426 mm ($Re \approx 1.34 \times 10^6$), and the full transition is achieved at the end of the measurement (561 mm).

The transition data of Mach 5.5A and 5.5B conditions are shown in Figure 4.3 and 4.4. For Mach 5.5A, the transition initiates at 156 mm with the turbulent spot [19] and completes transition at approximately 277.5 mm. The transition Reynolds number equates to $Re \approx 2.54 \times 10^6$. Even though the freestream pressure is almost similar for Mach 7A and Mach 5.5A conditions, the transition Reynolds number is smaller for Mach 7A condition, suggesting that the higher temperature of freestream could shift the transition location. The transition distance between the transition onset and the full transition (120 mm)

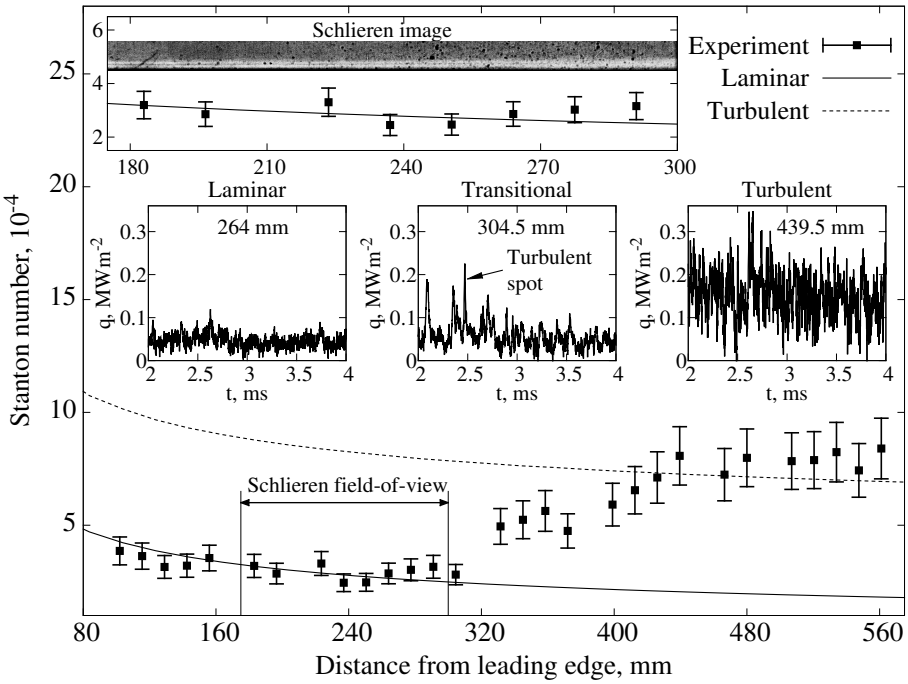

Figure 4.1: Surface heating loads along the flat plate: Mach 7A.

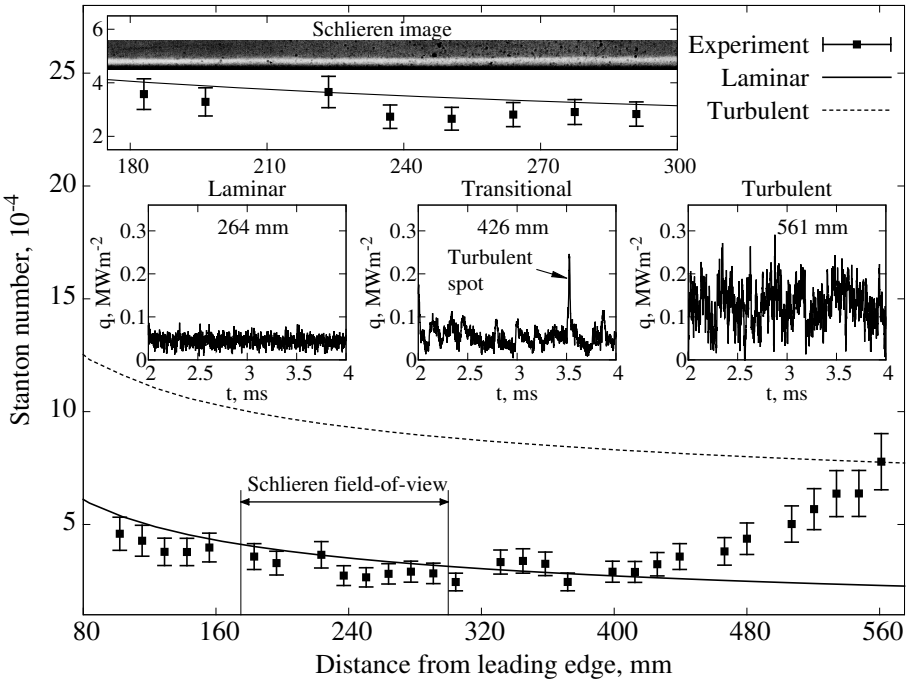

Figure 4.2: Surface heating loads along the flat plate: Mach 8A.

for the Mach 5.5A condition is $Re \approx 1.1 \times 10^6$. For Mach 5.5B, the onset of transition is shifted upstream to 129 mm, and the full turbulence is achieved at 210 mm ($Re \approx 2.88 \times 10^6$). With a shorter transition distance than the Mach 5.5A, the Mach 5.5B condition has almost the same transition distance in terms of Reynolds number ($Re \approx 1.11 \times 10^6$). Both Mach 5.5 enthalpy conditions displayed longer transition Reynolds numbers than those of Mach 7 and 8 enthalpy conditions, suggesting that freestream enthalpy effect in boundary layer transitions.

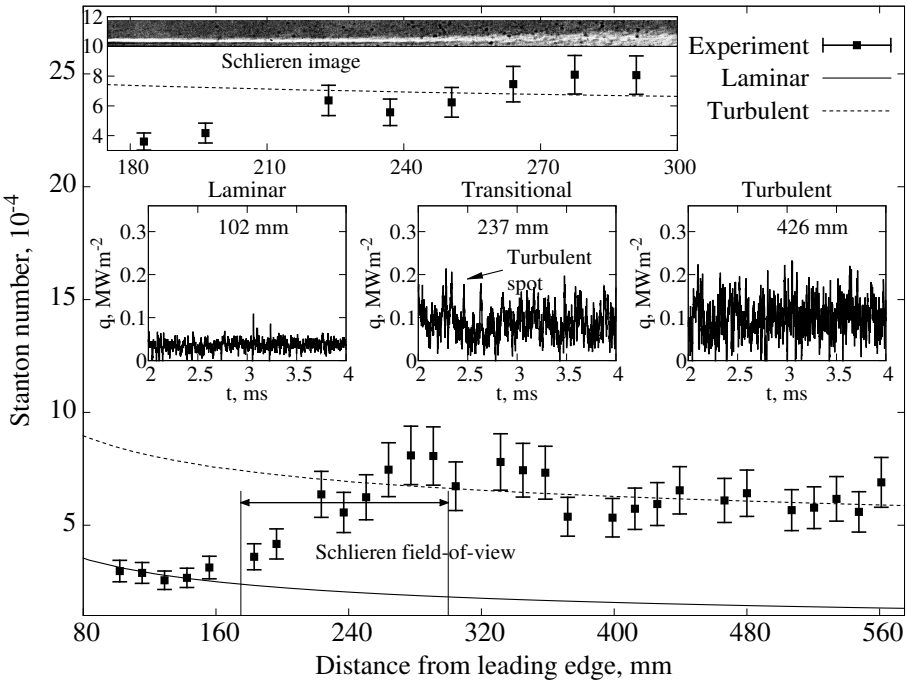

Figure 4.3: Surface heating loads along the flat plate: Mach 5.5A.

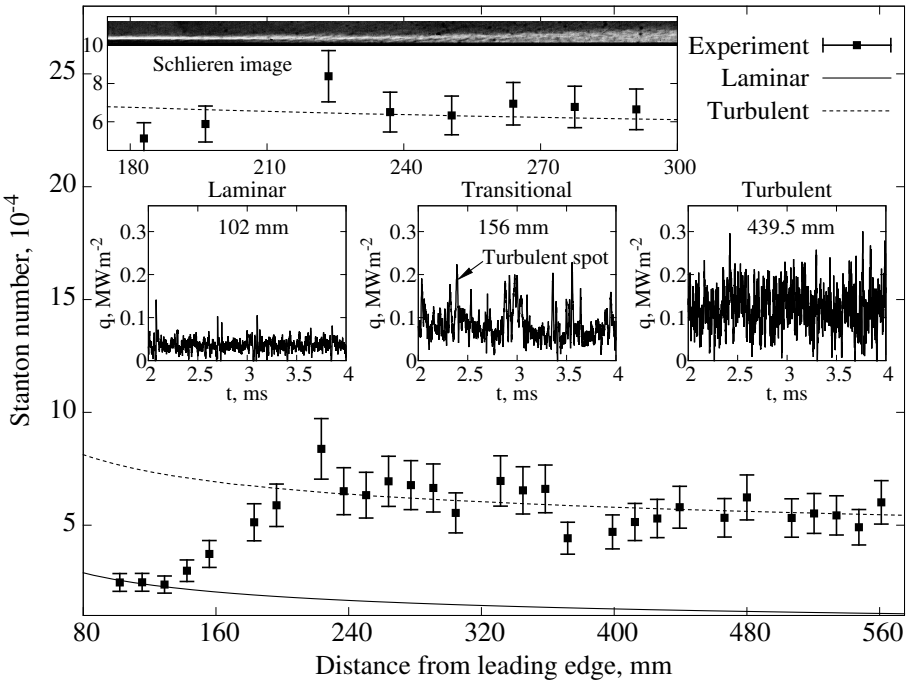

Figure 4.4: Surface heating load along the flat plate: Mach 5.5B.

4.1.2 Tripped Boundary Layer Results

Next, the effect of the boundary layer trip was examined. Although the disturbance from the trip would induce shock waves, the downstream surface pressure captured in Fig. 4.5 was almost similar to the untripped case. Instead, the effect of boundary-layer trip is clearly captured in Fig. 4.6. The trip creates vortices that leads to a significant thickening of the boundary layer in the schlieren images. The vortices also led to a rise in heat-transfer downstream of the trip (102 mm), but the heat-transfer level is smaller

and less chaotic than the fully turbulent signals. Although the trip did not achieve an immediate transition to turbulence, the averaged Stanton number increases gradually, depicting a "hypersonic delay" distance from the location of the boundary layer trip (60 mm) to a fully turbulent level at 223.5 mm. By using the trip, the transition Reynolds number had advanced from 2.16 $\times$ 10^6 to 1.08 $\times$ 10^6.

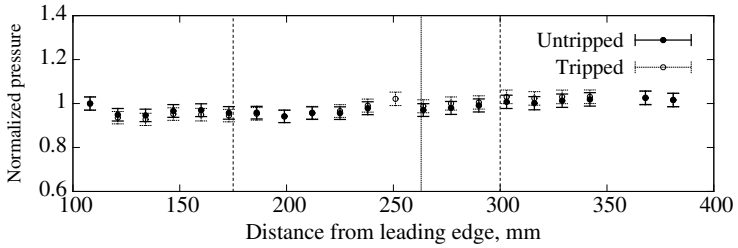

Figure 4.5: Effect of boundary layer trip: Mach 7A pressure.

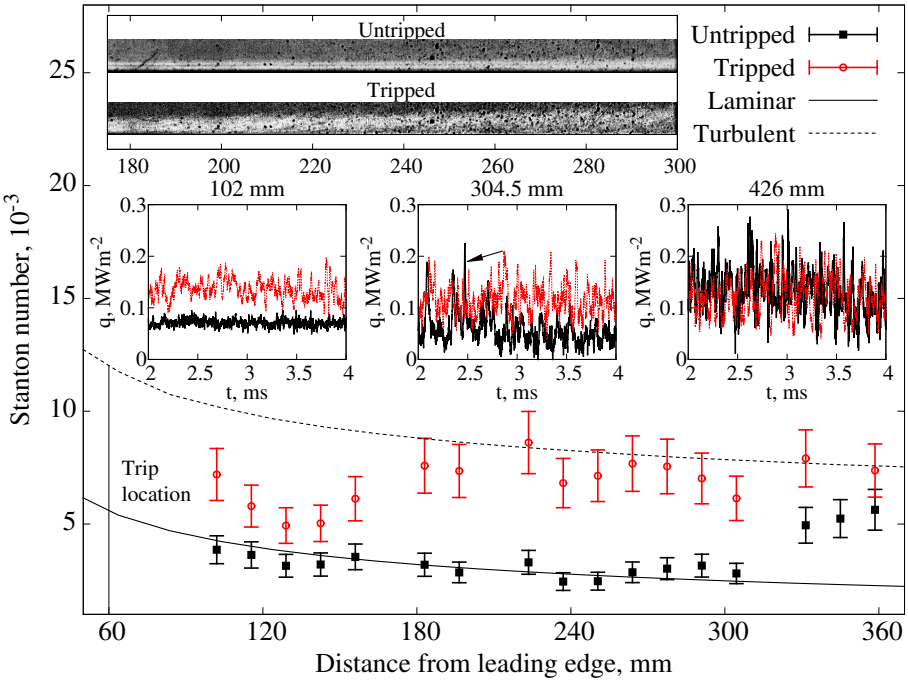

Figure 4.6: Effect of boundary layer trip: Mach 7A Stanton number.

The tripped results of Mach 5.5A condition in Fig. 4.7 show an upstream transition with the higher Re_∞. The Stanton number of the untripped boundary layer is laminar at 102 mm. In contrast, the Stanton number and the heat-transfer level of the tripped configuration get very near to the theoretical fully turbulent distribution. The tripped boundary layer becomes fully turbulent at 156 mm or $Re \approx 1.42 \times 10^6$. The untripped boundary layer, however, only captures turbulent spots at 183 mm. The tripped Mach 5.5A results display a much shorter physical "hypersonic delay" distance than the Mach 7A results yet in terms of Reynolds number the Mach 5.5A value is higher ($Re \approx 8.79 \times 10^5 > Re \approx 6.97 \times 10^5$). This delay in transition in previous T4 experiments [52] was measured to be a Reynolds number of 1-1.5 $\times$ 10^6, which equates to $\approx$ 150 mm. The delay is $\approx$ 150 mm, which is shorter in the present work.

4.1.3 CFLDI - Unheated

Four different trip heights were used to test the effects that different sized boundary layer trips have on a Mach 7.3 flat plate boundary layer. Schlieren imaging was used to visually characterise the boundary

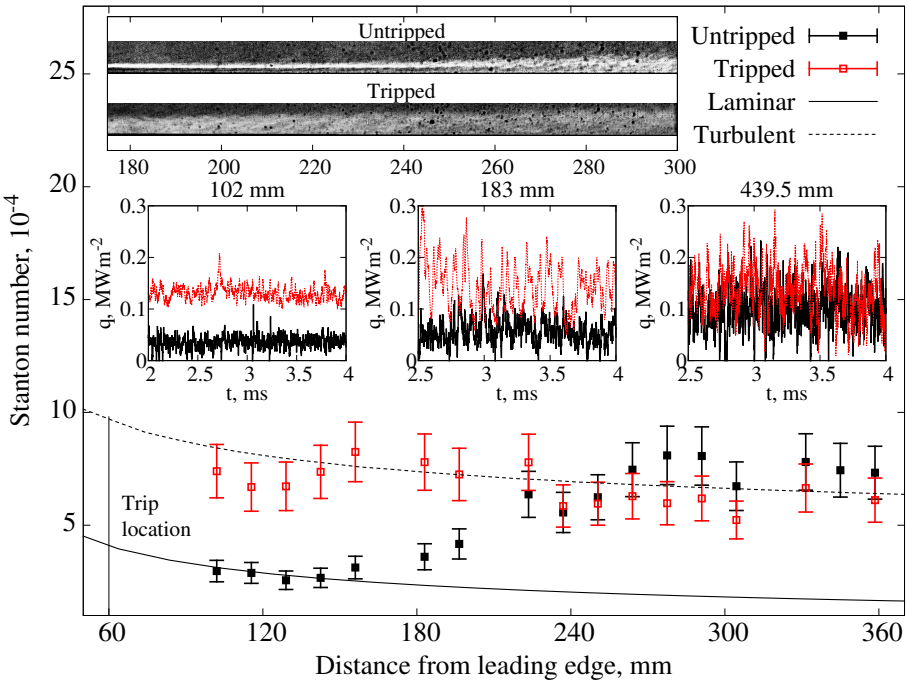

Figure 4.7: Effect of forced-transition: Mach 5.5A Stanton number.

layer flow field for the untripped, 1.4 mm and 2.0 mm tripped boundary layer configurations. Figure 4.8 shows schlieren images averaged over a series of frames and then post processed to allow easy distinction of the boundary layer height. Objects of known dimensions were placed in the schlieren field of view to allow for the pixel to distance ratio to be calculated and used to measure the boundary layer heights [47, 58].

Table 4.1 shows the measured heights of the various configurations and their associated uncertainty as well as the calculated boundary layer heights using the peak frequency measured from the CFLDI. It is seen that the effect of a boundary layer trip increases the height of the boundary layer by 50%. However, an increase in trip height does not appear to vary the boundary layer thickness substantially as seen in Table 4.1. A common boundary layer trip parameter is the ratio of the trip height (k) to the height of the boundary layer (δ) at the location of the trip. The Cebeci equations from [59] have been used to calculate the height of the laminar boundary layer 60 mm from the leading edge. The Cebeci method solves the coupled mass, momentum and energy equations for external laminar and turbulent flows. Figure 4.9

Table 4.1: Measured boundary layer heights.

Shot	Configuration	k/δ	δ_m (mm)	f_m (kHz)	$f_m\delta_m/u_\infty$	δ_c (mm)	$f_m\delta_c/u_\infty$
A	Untripped	0.0	4.4 ± 0.8	308	0.735	–	–
B	1.4 mm Trip	1.9	7.0 ± 0.8	196	0.745	–	–
C	2.0 mm Trip	2.7	6.3 ± 1.5	247	–	5.5 ± 0.6	0.74
D	3.0 mm Trip	4.0	–	200	–	6.8 ± 0.8	0.74

shows the pressure gradient along the length of the plate for the various trip configurations. An increase in trip height corresponds to a slight increase in surface pressure. Using the measured heat transfer and

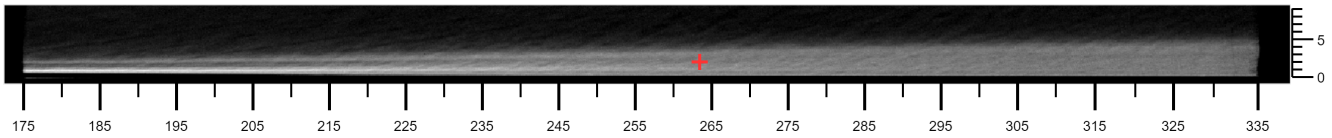

(a) Untripped boundary layer state.

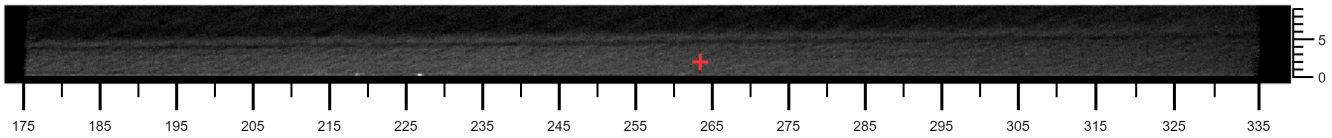

(b) 1.4 mm ($k/\delta = 1.9$) tripped boundary layer state.

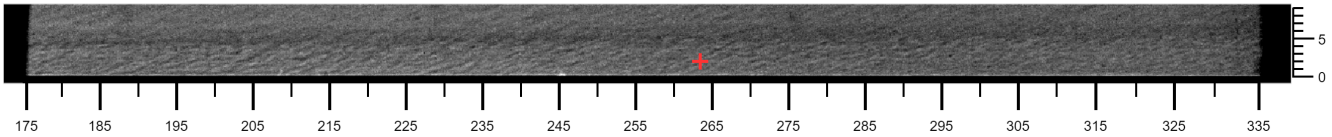

(c) 2.0 mm ($k/\delta = 2.7$) tripped boundary layer state.

Figure 4.8: Boundary layer state for different model configurations, with the CFLDI probing location superimposed in red (flow travelling from left to right). Units in mm.

tunnel conditions, the Stanton number distribution along the length of the plate can be calculated using:

$$St = \frac{\dot{q}}{\rho_\infty u_\infty \Delta h} \tag{4.1}$$

The Stanton numbers have an uncertainty of 11%, a detailed explanation of the associated uncertainty can be found in Appendix B5 of [60]. Using the same Cebeci code mentioned previously, the laminar and turbulent theoretical Stanton numbers are plotted with the measured values shown in Figure 4.10. The configurations with boundary layer trips have high amounts of heat transfer after the trip which decreases with increasing distance from the leading edge. From approximately 225 mm, the Stanton numbers of the tripped cases sit below the theoretical turbulent value. The Stanton number of the untripped case rise above laminar values at approximately 185 mm and then reach turbulent values at around 250 mm, where it sits consistently above the tripped cases. The decrease in heat transfer is due to the thickening of the boundary layer which reduces the steepness of the temperature gradient near the wall.

Cylindrically focused laser differential interferometry measurements were taken inside the boundary layer to analyse the turbulent fluctuations. Turbulence is generally diagnosed by two characteristics, the turbulent intensity and the frequency spectrum. The turbulent intensity is the percentage of velocity fluctuations to the mean value as given by:

$$TI\% = \frac{u'_{RMS}}{u_\infty} \times 100\% \tag{4.2}$$

The strong Reynolds analogy can be used to relate the density fluctuations measured by CFLDI to the velocity fluctuations used to calculate the turbulent intensity using [38]:

$$\frac{\rho'}{\bar{\rho}} = (\gamma - 1) M^2 \frac{u'_{RMS}}{u_\infty} \tag{4.3}$$

Hypersonic boundary layers are known to have high frequency disturbances due to the nature of the breakdown of laminar flow into turbulence. Using the turbulent intensity to directly compare turbulence between high speed flows has some limitations. The value is more sensitive to variations in the

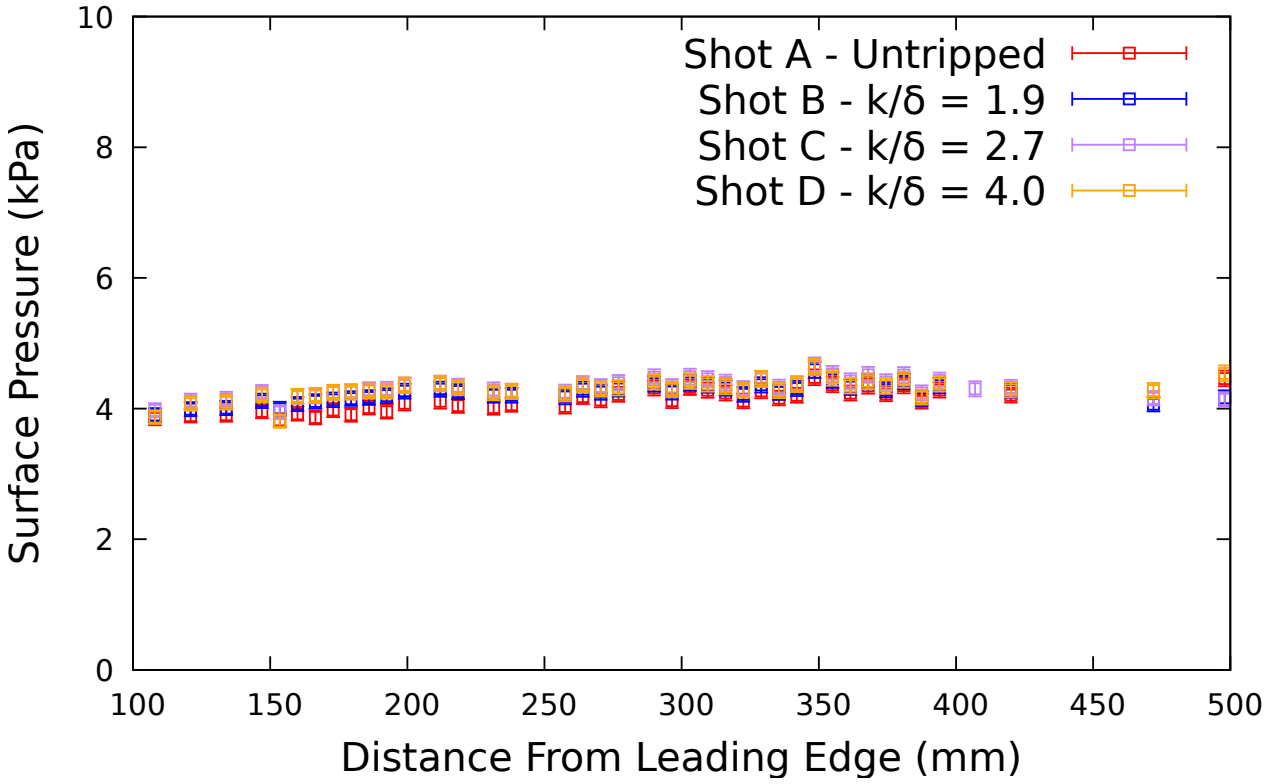

Figure 4.9: Steady test time surface pressure measurements along the flat plate.

lower time scale disturbances compared to higher time scale disturbances. Qualitative and quantitative analysis of the disturbance spectra allows for a more fair comparison of higher frequency turbulence to be made between flows. The CFLDI system is insensitive to the absolute density at the focal point and is only able to detect the gradient between the two closely separated points [39]. This means that the mean density cannot be calculated and used to find the turbulent intensity in this investigation. Therefore the analysis presented within this investigation will use the disturbance spectrum to compare results between different configurations.

The focal point of the CFLDI system was at the location 1.75 mm above the model's wall. The power spectral density graphs are estimated using Welch's method with Blackman windows of 1000 points and 50% overlap. Signal-to-noise ratios of 18 and 5-8 were achieved for the untripped and tripped cases respectively. Figure 4.11 shows the density fluctuations spectrum of each configuration normalised by each shot's density RMS value. This is done to account for the difference in voltage magnitudes measured by each test, allowing for the shape of each spectra to be compared. Analysing the shape of the spectra shows that above 150 kHz all four configurations match very well. This gives an indication that the trips have little to no effect on the higher frequency distribution in this region of the boundary layer. A line with a gradient of -5/3 representing the Kolomogorov roll-off is superimposed on the plot and matches quite well with the CFLDI results. Figure 4.12 shows the density fluctuation spectrum of each configuration normalised by Shot A's density RMS value as a baseline case to compare against. It showed that increasing the trip height had little to no effect on the downstream density fluctuations, while the introduction of a boundary layer trip reduced the magnitude of the density fluctuations above 100 kHz. Large eddy simulations conducted by Wang et al. [61] show the magnitude of the density fluctuations inside a hypersonic boundary layer to decreases with increasing distance downstream from the transition location. It also shows that the turbulent fluctuations reach a peak in the lower region of the boundary layer and decrease towards the boundary layer edge. The CFLDI probing location was kept constant for the tripped and untripped cases. The increase in boundary layer height due to the

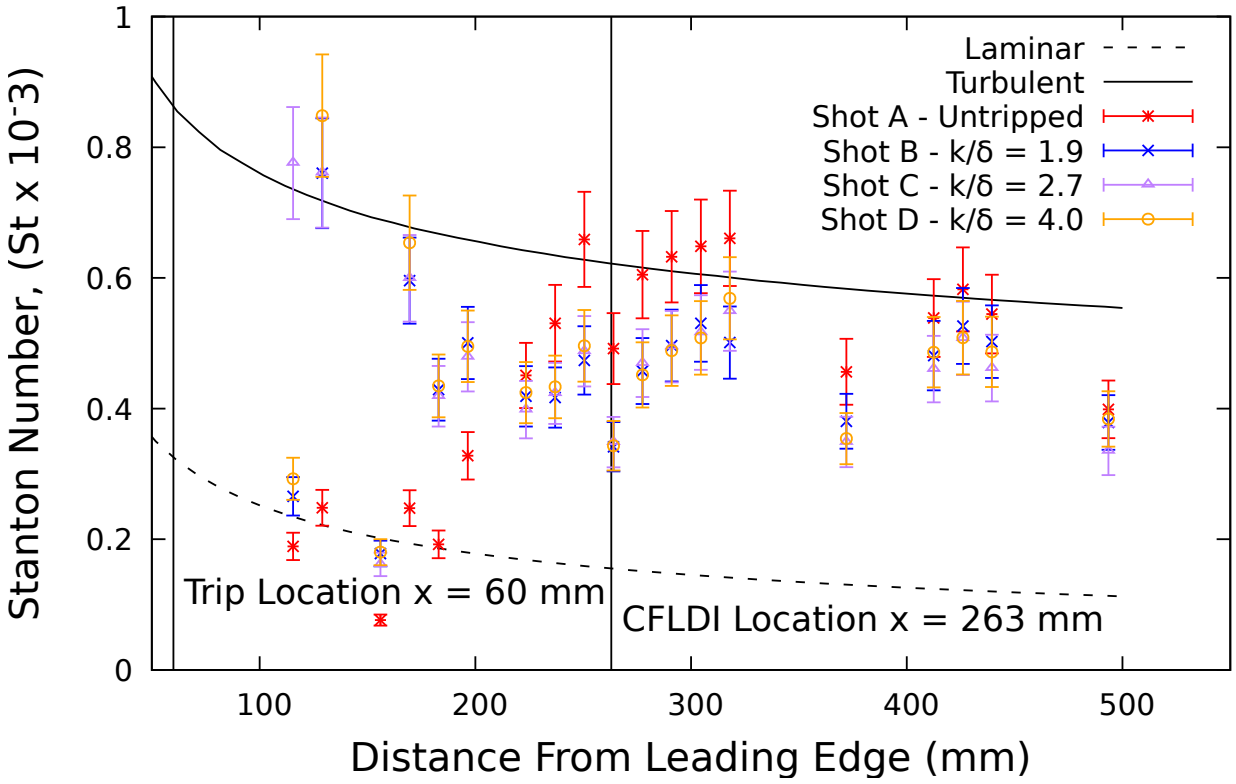

Figure 4.10: Mach 7.3 surface heat transfer measurements for the tripped and untripped cases.

trips meant the tripped cases were probed at a lower y/δ than the untripped case. This would suggest that the tripped cases should have larger density fluctuations, however, the results show the opposite to be true. The trips are believed to produce a turbulent boundary layer that mimics a naturally transitioned boundary layer at a large distance downstream from the transition location. As Wang et al. [61] found, the magnitude of density fluctuations decreases with increasing distance downstream from the transition location, which indicates that the tripped cases should experience a decrease in density fluctuations. This is believed to be the greater effect explaining why a decrease in density fluctuations at the same location is observed when trips are used. The mean density value at the probing location was not measured during this campaign, therefore the turbulent intensity could not be determined and used to compare each case. Analysis of the peak frequencies using the scaling relation ($f \propto u_\infty/\delta$) allow estimates of the boundary layer thickness to be made [17]. Table 4.1 shows the peak frequency decreases when a boundary layer trip is added to the flow, which agrees with the increase in boundary layer height seen in the schlieren images. Using the schlieren and CFLDI results of shots A and B, an average proportionality constant can be found and used to estimate the boundary layer height for shots C and D (shown in Table 4.1). The estimated boundary layer height for shot C is less than the measurement taken from the schlieren images, however, it is still within the bounds of uncertainty. The estimated thickness of shot D is larger than shot A and within the vicinity of shots B and C so this result is reasonable.
Analysis of shot D's spectra shows a large peak at 900 kHz. The peak at 900 kHz is observed to occur before the test flow arrival as seen in Figure 4.13. Another peak at 1.8 MHz is also present before flow arrival but does not appear during the test time due to its smaller magnitude. These peaks are believed to be due to signals of nearby AM radio stations or are a feature of the laser used.

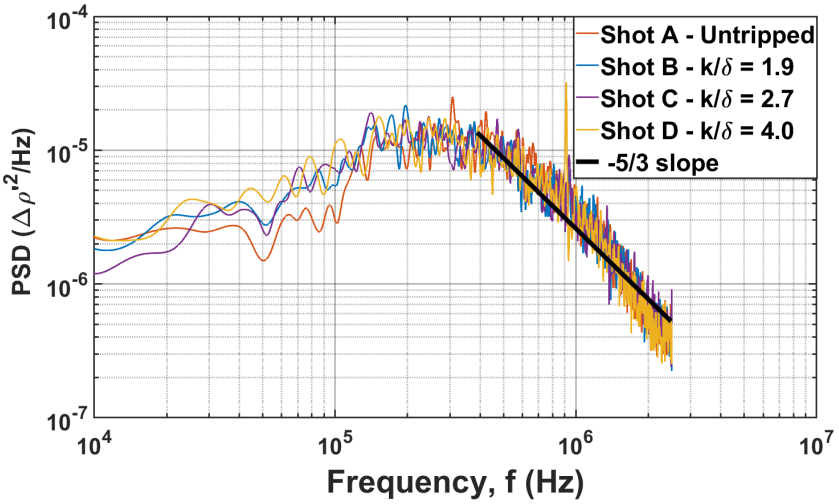

Figure 4.11: Density fluctuation spectra inside the boundary layer.

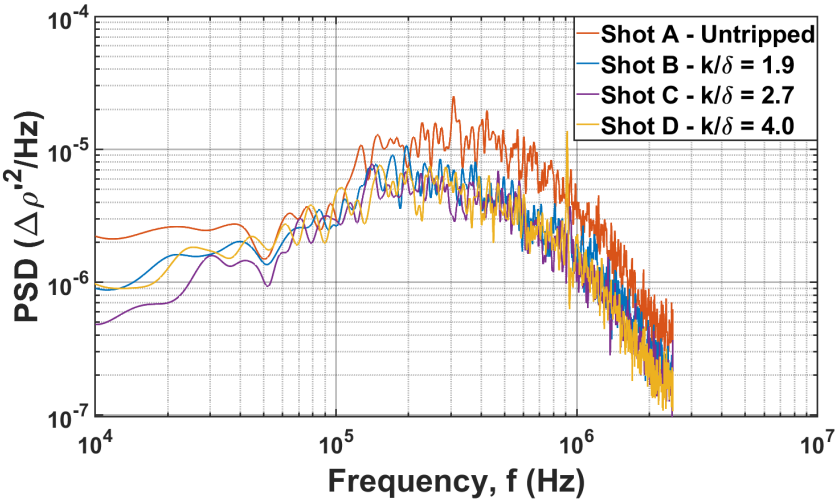

Figure 4.12: Density fluctuations spectra inside the boundary layer normalised by shot A.

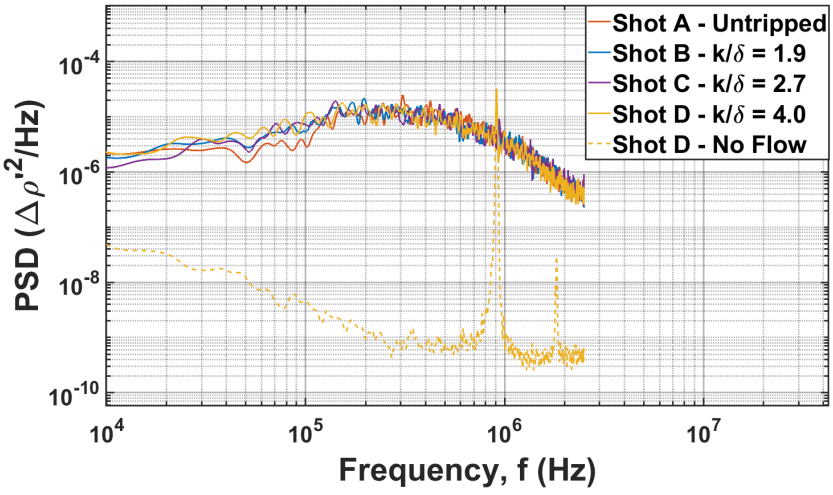

Figure 4.13: Density fluctuations spectra inside the boundary layer with shot D before flow data.

4.2 Heated Model Results

4.2.1 Heated Model Schlieren Results

Wall heating was performed to achieve different temperatures for the shock-tunnel testing. Fig. 4.14 displays the IR images recorded immediately before the shot. For safety reasons, the power supply was switched off immediately before firing the tunnel. Because there were extra time delays ($\approx$ 15 s) between the power switch-off and the shot, the temperature levels were lower than those from static testing shown in Fig. 2.17. Taking the mean surface temperature of the image's field-of-view, the T_w/T_0 achieved ≈ 0.3 for a couple of sample conditions presented below (Mach 7 and Mach 5.5 enthalpy conditions).

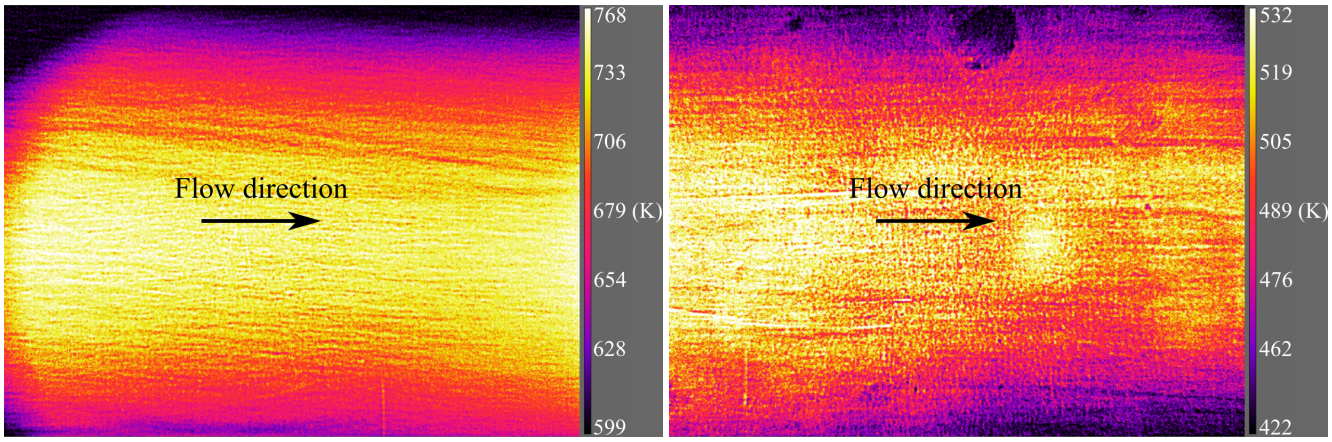

(a) Mach 7 enthalpy, $T_w \approx 720$ K (b) Mach 5.5 enthalpy, $T_w \approx 500$ K

Figure 4.14: IR images from the shock tunnel tests.

Figures 4.15 and 4.16 show post-processed schlieren images of the flat plate boundary layer captured during the test-time at 3 ms from the nozzle-supply pressure trigger. The images have been post-processed to enhance the boundary layer structures. For all images, the flow direction is from left to right, with the wall marked as a red line in each image. The horizontal scale is the streamwise distance from the leading edge in millimetres. Image post-processing adjusted the contrast to enhance the boundary layer structures. The flow patterns captured near the unheated wall in Fig. 4.15(a) show a relatively even profile near the wall, indicating the boundary layer of the Mach 7 enthalpy flow predominately stays laminar in this field-of-view. Approximately 285 mm (Re $\approx 1.43 \times 10^6$) downstream of the leading edge, the density gradient starts to show an uneven profile with thickening of the boundary layer. This indicates that the boundary layer is becoming unstable.

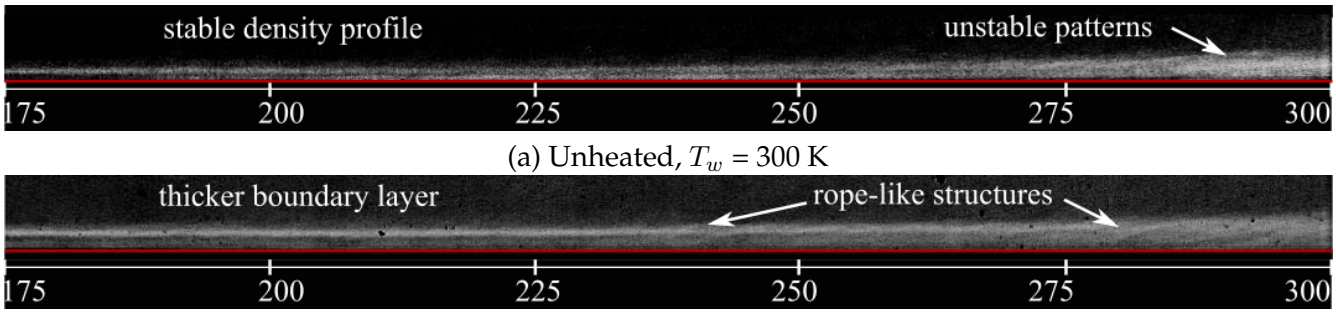

(a) Unheated, T_w = 300 K

(b) Heated, $T_w \approx 720$ K

Figure 4.15: Flat plate schlieren - Mach 7A, $Re_\infty = 5.06 \times 10^6$ 1/m.

When the surface is heated to higher wall temperatures as shown in Fig. 4.15(b), the boundary layer gets thicker, indicating a discernible growth of the boundary layer at hot-wall conditions relative to the

unheated case. The diagonal flow patterns between 240 and 280 mm are possibly the "rope-like" structures [34] starting to form due to instabilities in the boundary layer. It seems that the "rope-like" structures form further upstream in the heated case compared to the unheated case, leading to an increased level of transitional/turbulent boundary layer structures at a given position.

Compared to the flow patterns observed in the Mach 7 enthalpy flow, the boundary layer patterns of the Mach 5.5 enthalpy flow in Fig. 4.16 are significantly different. For the unheated case captured in Fig. 4.16(a), the "rope-like" structures also form and become visible. The turbulent structure thickens and is fully established at the downstream section. The chaotic flow structures are due to the higher Reynolds number of the flow causing the boundary layer to transition upstream. Fig. 4.16(b) shows that, when the wall is heated to higher temperatures, the turbulent boundary layer structure becomes thicker as well. Compared to Fig. 4.15(b), Fig. 4.16(b) has more crisp and distinct turbulent structures in the heated boundary layer.

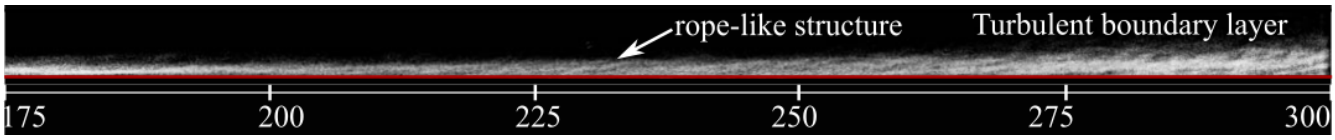

(a) Unheated, T_w = 300 K

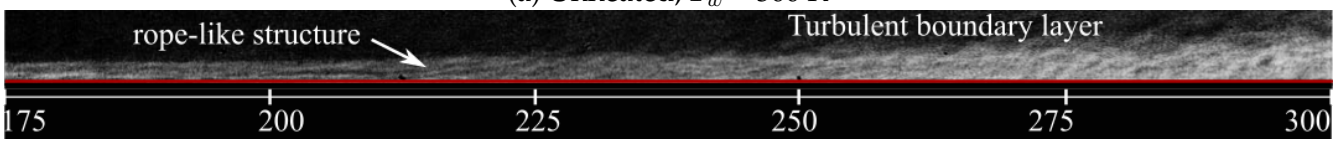

(b) Heated, $T_w \approx$ 500 K

Figure 4.16: Flat plate schlieren - Mach 5.5A, $Re_\infty = 9.58 \times 10^6$ 1/m.

Regarding the boundary layer transition, previous flat plate studies in T4 measured the transition Reynolds number as large as 1.43×10^6 for the flow enthalpy of 2.45 MJ/kg [18] and 1.5×10^6 for the flow enthalpy of 5.2 MJ/kg [19]. The transition Reynolds number of 1.43×10^6 corresponds to a distance of 283 mm and 157 mm from the leading edge for the Mach 7 enthalpy and Mach 5.5 enthalpy conditions, respectively. The unstable patterns apparent in the vicinity of 283 mm in Fig. 4.15 and the start of the field-of-view in Fig. 4.16 indicate transition. To better characterise the growth of the boundary layer, the boundary layer height along the field-of-view was measured semi-numerically and plotted in Fig. 4.17. This was accomplished by averaging the schlieren images during steady test-time and normalising the intensity value for each pixel to be between 0 and 1. A threshold limit is set where any pixel intensity below the value is set to 0 (black) and any above is set to 1 (white). For each column of pixels normal to the wall, the boundary layer height was the distance between the first and last white pixel. A Gaussian filter (σ = 6) was then applied to smooth the noise of the boundary layer height. In Figs. 4.17(a) and (b), the experimental data confirms the growth of the boundary layer with high wall temperatures. The measured boundary layer height from wall heating in Fig. 4.17(a) increases by 41 and 42% at 185 and 250 mm from the leading edge, respectively. In Fig. 4.17(b), the boundary layer thickens by 28 and 35% for the same streamwise locations. In this work, the authors consider the major source of the error in measurement occurred from determining the edge of the boundary layer. Shaded regions in each of the plots represent variations of boundary layer height from a range of threshold limits. Due to the chaotic flow structure of transition/turbulent boundary layer, edge detection of all plots in the downstream field-of-view showed larger variation from the threshold. For each unheated and heated wall case, an approximated boundary layer thickness calculated by Cebeci [62] boundary layer program [52] is overlaid in Fig. 4.17. The program uses the coupled laminar and turbulent boundary layer equations with a user-specified transition location. For the results presented herein, transition was initiated at streamwise locations achieving transitional Reynolds number using previous flat plate correlations in T4. A comparison between experimental data and numerical approximation showcases

that Schlieren-based measurement could reasonably capture the structure of the hypersonic flat plate boundary layer.

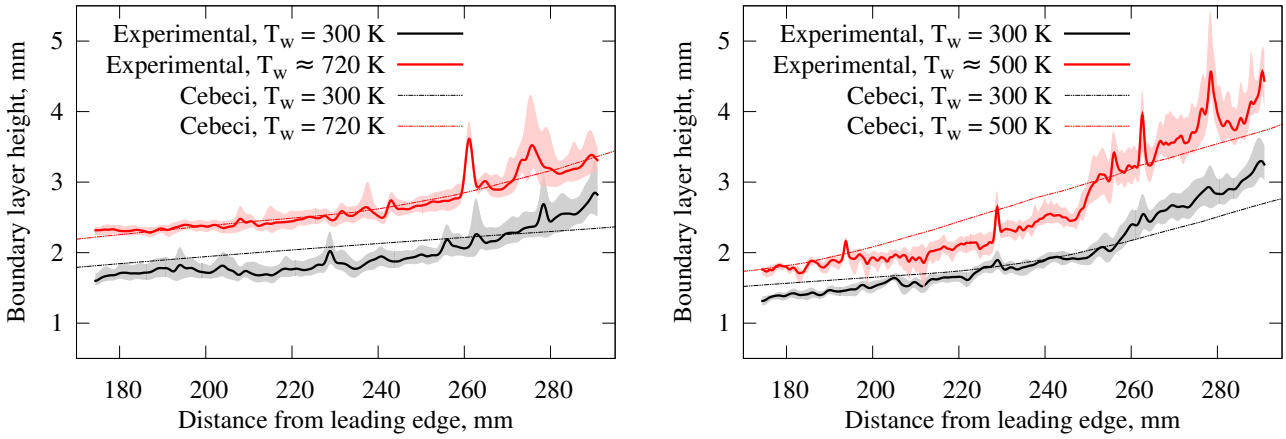

(a) Mach 7 enthalpy (b) Mach 5.5 enthalpy

Figure 4.17: Measured boundary layer heights from the wall heating.

Determining the exact transition onset location over the heated wall proved to be somewhat challenging with the current test apparatus. This was primarily because the line-of-sight schlieren captures an integrated density gradient over the width of the model. To better understand the effects of wall heating in boundary layer transition, further quantitative analysis of the experimental data is required. Measuring surface heat transfer with closely-spaced thin-film heat-transfer gauges [52] could give a direct indication of the transition location; however, the surface imperfections generated by such instrumentation would lead to temperature non-uniformities within the heated plate.

CFLDI - Heated

Finally, we undertook some recent tests using the CFLDI set-up with the heated model. These results are being analysed at present, even though the project has been completed. We expect to report the finalised results in archived, peer-reviewed articles in the coming months. Below, we present some of the initial results from this test campaign. The plate was heated to around 900K and the CFLDI probe was set-up to interrogate the transitional region with flow conditions approximately at a unit Reynold's number of 5.4 million-per-metre.

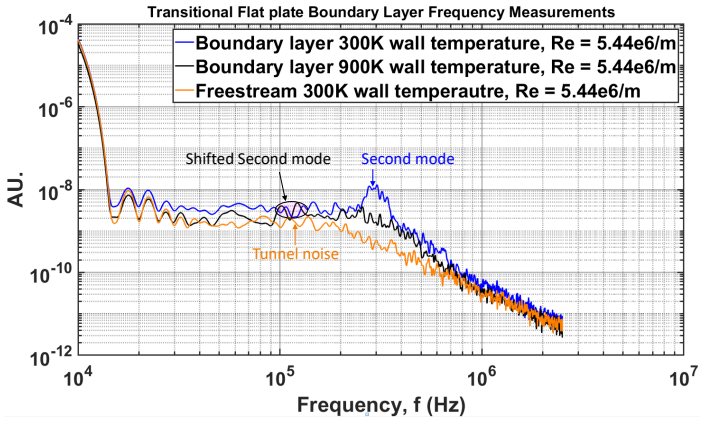

Figure 4.18: Density fluctuations spectra inside the boundary layer for three cases: a) unheated plate (blue) at 300K, b) heated plate (black) at 900K and c) tunnel spectra (orange).

A preliminary sample set of results shown in Figure 4.18 showcase how the second mode gets affected due to the heating. Based on stability theory, this is expected that the second mode frequencies will get lower and the amplitudes will also drop. However, it is interesting that this lowered frequency potentially matches with the tunnel frequencies. The ongoing analysis work will aim to check if heating indeed increases the receptivity of the boundary layer to the tunnel noise. This, if it is the case, will explain the counter intuitive results (that heating the plate has advanced the transition location and destabilised the boundary layer more rapidly) that we obtained in our previous year works via schlieren imaging [47].

Spectograms of the CFLDI data undertaken at three different temperatures at approximately the same test-condition versus test-time is presented in figure 4.19. They demonstrate a rich dynamics of response. For the unheated (300K) case, there is a consistent $\approx$ 300kHz tone that is captured by the measurements. For the 500K and the 800K cases, these are less defined and potentially indicate a strongly transitioning (500K case) and fully transitioned to turbulence (800K case) results. The strong signal for the 500K case at $\approx$ 1ms is likely from a small particle (like a part of the diaphragm) convecting through the boundary layer.

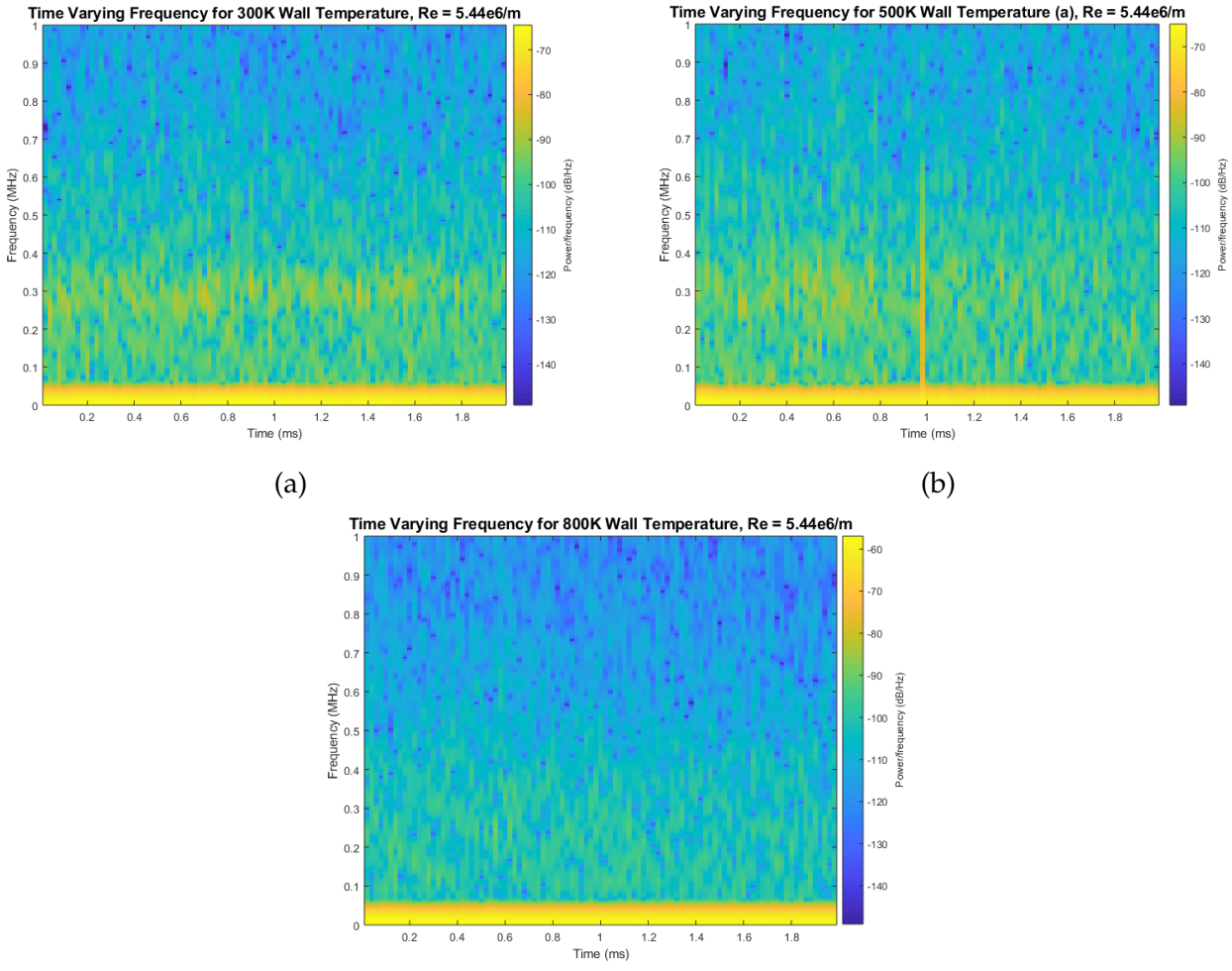

Figure 4.19: CFLDI spectograms vs test-time for three different wall temperatures: a) 300K, b) 500K and c) 800K.

5

Conclusions & Future Work

In this project, we successfully developed a heated flat-plate model and tested it in The University of Queensland's T4 Stalker tube. Schlieren imaging, surface pressure/heat transfer measurements and cylindrical focused laser differential interferometry were used to analyse the effects that wall heating had on the transition and growth of turbulence.

The schlieren images demonstrated that the heating thickened the boundary layer and caused it to transition earlier. CFLDI measurements showed that a predominant ≈300kHz tone is present for the unheated plate in the transition zone, whereas this drops to closer to ≈100kHz when heating of around 900K is applied. This seems to also match closer to the tunnel free-stream frequencies measured. These results will be analysed further to advance our understanding of how the wall temperature affects the boundary layer transition.

With an unheated model, we also undertook surface heat transfer and pressure measurements with and without boundary layer trips. The schlieren images of these tests showed an increase in boundary layer height of approximately 50% when boundary layer trips were present. Using the measured peak disturbance frequency for each case with CFLDI, an estimate for the boundary layer thickness was made. The estimated thicknesses were within the uncertainty of the heights detected in the schlieren images. Analysis of the boundary layer spectra showed that the trips had little to no effect on the shape of the higher frequency density fluctuations. Varying the height of the boundary layer trips also had little to no effect on the shape or the magnitude of the fluctuations. However, it was found that the addition of the trips decreased the magnitude of the density fluctuations above 100 kHz. This is believed to be caused by the trips promoting well-developed boundary layers downstream of their location. Direct comparison could not be made between the turbulent intensity of each configuration due to the mean density value not being estimated. A technique similar to [43] could also be used where the CFLDI system is focused to a line equal to the boundary layer thickness such that the total turbulence at the probing location can be measured.

In future work, we are proposing to investigate the development of tailored wall-temperature profiles in order to preferentially control the transition location. This will be demonstrated in a simple flat-plate geometry initially, and then deployed to more complex shapes such as the BOLT model.

Acknowledgements

We thank Dr. Sarah Popkin for supporting this grant via Project Number: FA9550-18-1-0265.

We also thank Prof. Hans Hornung (Caltech), Prof. Nick Parziale (Stevens Institute) and Prof. Stuart Laurence (Maryland) for their valuable insights and discussions that led to our developing first the FLDI capability and next the CFLDI capability for use in T4.

Publications List

Journal Articles

1. Chang, E.W.K., Chan, W.Y., Hopkins, K.J., McIntyre, T.J. and Veeraragavan, A., 2020. Electrically-heated flat plate testing in a free-piston driven shock tunnel. ***Aerospace Science and Technology***, 103, p.105856.

2. Chang, E.W.K., Chan, W.Y., McIntyre, T.J. and Veeraragavan, A., 2021. Hypersonic shock impingement on a heated flat plate at Mach 7 flight enthalpy. ***Journal of Fluid Mechanics***, 908 (Rapids-1).

3. Hopkins, K.J., Porat, H., McIntyre, T.J., Wheatley, V. and Veeraragavan, A., 2021. Measurements and analysis of hypersonic tripped boundary layer turbulence. ***Experiments in Fluids***, 62(8), pp.1-12.

Conferences

1. Chang, E.W.K., Chan, W.Y., McIntyre, T.J. and Veeraragavan, A., Hypersonic shock impingement on a heated surface in the T4 free-piston driven shock tunnel, ***32nd International Symposium on Shockwaves***, Singapore, 2019.

Bibliography

[1] Andrew Dann. The manufactoring of thin film heat trasnfer gauges. rev ii. Technical report, The University of Queensland, School of Mining and Mechanical Engineering, 2019.

[2] E. H. Hirschel. Thermal surface effects in aerothermodynamics. In *Proceedings of the 3rd European Symposium on Aerothermodynamics for space vehicles held at ESTEC*, volume 426 of *ESA Special Publication*, pages 17–31, Noordwijk, The Netherlands, 1998.

[3] Alexander Fedorov. Transition and stability of high-speed boundary layers. *Annual Review of Fluid Mechanics*, 43(1):79–95, 2011. doi: 10.1146/annurev-fluid-122109-160750.

[4] M Bleilebens and H Olivier. On the influence of elevated surface temperatures on hypersonic shock wave/boundary layer interaction at a heated ramp model. *Shock Waves*, 15(5):301–312, 2006. doi: 10.1007/s00193-006-0025-2.

[5] C. Fischer and H. Olivier. Experimental investigation of the internal flow field of a scramjet engine. In *16th AIAA/DLR/DGLR International Space Planes and Hypersonic Systems and Technologies Conference*, San Francisco, California, 2009. doi: 10.2514/6.2009-7369.

[6] C. Fischer and H. Olivier. Experimental investigation of the shock train in an isolator of a scramjet inlet. In *17th AIAA International Space Planes and Hypersonic Systems and Technologies Conference*, San Francisco, California, 2011. doi: 10.2514/6.2011-2220.

[7] C. Fischer and H. Olivier. Experimental investigation of wall and total temperature influence on a shock train. *AIAA Journal*, 52(4):757–766, 2014. doi: 10.2514/1.J052599.

[8] M. Bernardini, I. Asproulias, J. Larsson, S. Pirozzoli, and F. Grasso. Heat transfer and wall temperature effects in shock wave turbulent boundary layer interactions. *Physical Review of Fluids*, 1:1–18, December 2016. doi: 10.1103/PhysRevFluids.1.084403. URL `https://link.aps.org/doi/10.1103/PhysRevFluids.1.084403`.

[9] L Duan, I Beekman, and M. P. Martin. Direct numerical simulation of hypersonic turbulent boundary layers. part 2. effect of wall temperature. *Journal of Fluid Mechanics*, 655:419–445, 2010. doi: 10.1017/S0022112010000959.

[10] Xing-Kun Zhu, Chang-Ping Yu, Fu-Lin Tong, and Xin-Liang Li. Numerical study on wall temperature effects on shock wave/turbulent boundary-layer interaction. *AIAA Journal*, 55(1):131–140, 2017. doi: 10.2514/1.J054939.

[11] Jouke H. S. de Baar, Jai Vennik, and Andrew J Neely. Numerical study of the influence of non-uniform wall temperature distribution on the hypersonic flow over a flat plate. In *21st AIAA International Space Planes and Hypersonics Technologies Conference*, pages 1–15, Xiamen, China, 2017. doi: 10.2514/6.2017-2427.

[12] Will O Landsberg, Vincent Wheatley, Michael K Smart, and Ananthanarayanan Veeraragavan. Performance of high mach number scramjets-tunnel vs flight. *Acta Astronautica*, 146:103–110, 2018.

[13] James E Barth, Vincent Wheatley, and Michael K Smart. Effects of hydrogen fuel injection in a mach 12 scramjet inlet. *AIAA Journal*, 53(10):2907–2919, 2015. doi: 10.2514/1.J053819.

[14] W.O. Landsberg, A. Veeraragavan, and V. Wheatley. Characteristics of cascaded fuel injectors within an accelerating scramjet combustor. *AIAA Journal*, 54(12):1–9, 2016. doi: 10.2514/1.J054815.

[15] Will O. Landsberg, Nickolas N. Gibbons, V. Wheatley, Michael K. Smart, and Ananthanarayanan. Veeraragavan. Improving scramjet performance through flow field manipulation. *Journal of Propulsion and Power*, 54(12):1–9, 2017. doi: 10.2514/1.B36772.

[16] Augusto. F. Moura, Vincent Wheatley, and Ingo Jahn. Thermofluidic compression effects to achieve combustion in a low-compression scramjet engine. *Shock Waves*, December 2017. ISSN 1432-2153. doi: 10.1007/s00193-017-0782-0. URL `https://doi.org/10.1007/s00193-017-0782-0`.

[17] Kenneth F. Steston and Roger L. Kimmel. Surface temperature effects on boundary-layer transition. *AIAA Journal*, 30(11):2782–2783, 1992. doi: 10.2514/3.11300.

[18] Y. He and Richard G Morgan. Transition of compressible high enthalpy boundary layer flow over a flat plate. *The Aeronautical Journal*, 98(972):25–34, 1994. doi: 10.1017/S0001924000050181.

[19] David J Mee. Boundary-layer transition measurements in hypervelocity flows in a shock tunnel. *AIAA Journal*, 40(8):1542–1548, 2002. doi: 10.2514/2.1851.

[20] Dylan J. Wise and Michael K. Smart. Roughness-induced transition of hypervelocity boundary layers. *Journal of Spacecraft and Rockets*, 51(3):847–854, 2014. doi: 10.2514/1.A32674.

[21] Leslie M. Mack. Boundary-layer linear stability theory. techreport 709, Jet Propulsion Laboratory California Institue of Technology, 1984.

[22] Steven P. Schneider. Effects of high-speed tunnel noise on laminar-turbulent transition. *Journal of Spacecraft and Rockets*, 38(3):323–333, 2001.

[23] PS Klebanoff and KD Tidstorm. Mechanism by which a two-dimensional roughness element induces boundary-layer transition. *The Physics of Fluids*, 15(7):1173–1188, 1972.

[24] E Reshotko. Roughness-induced transition growth in a flat-plate boundary layey. In *40th AIAA aerospace sciences meeting and exhibit*, Reno, Nevada, 2002.

[25] Scott A. Berry, Aaron H. Auslender, Arthur D. Dilley, and John F. Calleja. Hypersonic boundary-layer trip development for Hyper-X. *Journal of Spacecraft and Rockets*, 38(6):853–864, 2001. doi: 10.2514/2.3775.

[26] E. R. Van Driest and W. D. McCauley. The effect of controlled three-dimensional roughness on boundary-layer transition at supersonic speeds. *Journal of the Aeronautical Sciences*, 27(4):261–271, apr 1960.

[27] Dyaln J. Wise and Michael K. Smart. Roughness-induced transition of hypervelocity boundary layers. *Journal of Spacecraft and Rockets*, 51(3):847–854, jun 2014.

[28] Katya M. Casper, Heath B. Johnson, and Steven P. Schneider. Effect of freestream noise on roughness-induced transition for a slender cone. *Journal of Spacecraft and Rockets*, 48(3):406–413, jun 2011.

[29] Leslie M Mack. Linear stability theory and the problem of supersonic boundary-layer transition. *AIAA journal*, 13(3):278–289, 1975. doi: 10.2514/3.49693.

[30] J Leith Potter. Review of the influence of cooled walls on boundary-layer transition. *AIAA Journal*, 18(8):1010–1012, 1980. doi: 10.2514/3.7703.

[31] Alexander Fedorov, Vitaly Soudakov, Ivan Egorov, Andrey Sidorenko, Yury Gromyko, Dmitry Bountin, Pavel Polivanov, and Anatoly Maslov. High-speed boundary-layer stability on a cone with localized wall heating or cooling. *AIAA Journal*, 53(9):2512–2524, 2015. doi: 10.2514/1.J053666.

[32] S. J. Laurence, A. Wagner, K. Hannemann, V. Wartemann, H. Lüdeke, H. Tanno, and K. Itoh. Time-resolved visualization of instability waves in a hypersonic boundary layer. *AIAA Journal*, 50(1): 243–246, jan 2012. doi: 10.2514/1.j051112.

[33] S. J. Laurence, A. Wagner, and K. Hannemann. Schlieren-based techniques for investigating instability development and transition in a hypersonic boundary layer. *Experiments in Fluids*, 55(8), jul 2014. doi: 10.1007/s00348-014-1782-9.

[34] Stuart J. Laurence, Alexander Wagner, and Klaus Hannemann. Experimental study of second-mode instability growth and breakdown in a hypersonic boundary layer using high-speed schlieren visualization. *Journal of Fluid Mechanics*, 797:471–503, 2016. doi: 10.1017/jfm.2016.280.

[35] Joel M Lawson, Mallory C Neet, Ilan J Grossman, and Joanna M Austin. Characterization of a focused laser differential interferometer. In *AIAA Scitech 2019 Forum*, page 2296, 2019.

[36] Joel M Lawson and Joanna M Austin. Expansion tube freestream disturbance measurements using a focused laser differential interferometer. In *AIAA Scitech 2020 Forum*, page 1064, 2020.

[37] Nick J. Parziale, Joseph E. Shepherd, and Hans G. Hornung. Differential interferometric measurement of instability in a hypervelocity boundary layer. *AIAA Journal*, 51(3), March 2013. doi: 10.2514/1.J052013.

[38] M. Fulghum. *Turbulence Measurements in High-Speed Wind Tunnels using Focusing Laser Differential Interferometry*. PhD thesis, The Pennsylvania State University, College of Engineering, 2014.

[39] B. E. Schmidt and J. E. Shepherd. Analysis of focused laser differential interferometry. *Applied Optics*, 54(28):8459, sep 2015. doi: 10.1364/ao.54.008459.

[40] Andrew P. Ceruzzi, Braeden O. Callis, Danial C. Weber, and Christopher P. Cadou. Application of focused laser differential interferometry in a supersonic boundary layer. In *AIAA SciTech Forum*, January 2020. doi: 10.2514/6.2020-1973.

[41] S Leonov A Houpt. Focused laser differential interferometer for supersonic boundary layer measurements on flat plate geometries. In *2018 Plasmadynamics and Lasers Conference*. American Instutue of Aeronautics and Astronautics, June 2018.

[42] Alec Houpt and Sergey Leonov. Focused and cylindrical-focused laser differential interferometer characterization of sbr-50 at mach 2. In *AIAA Aviation 2019 Forum, Dallas Texas*, 2019.

[43] Joshua M Weisberger, Brett F Bathel, Gregory C Herring, Gregory M Buck, Stephen B Jones, and Angelo A Cavone. Multi-point line focused laser differential interferometer for high-speed flow fluctuation measurements. *Applied Optics*, 59(35):11180–11195, 2020.

[44] Keill J Hopkins, Hadas Porat, Timothy J McIntyre, Vincent Wheatley, and Ananthanarayanan Veeraragavan. Measurements and analysis of hypersonic tripped boundary layer turbulence. *Experiments in Fluids*, 62(8):1–12, 2021.

[45] Wilson Y. K. Chan, Peter A. Jacobs, Michael K. Smart, Samuel Grieve, Christopher S. Craddock, and Luke J. Doherty. Aerodynamic design of nozzles with uniform outflow for hypervelocity ground-test facilities. *Journal of Propulsion and Power*, 34(6):1467–1478, 2018. doi: 10.2514/1.B36938.

[46] Ray J. Stalker, Allan Paull, David J. Mee, Richard G. Morgan, and Peter A. Jacobs. Scramjets and shock tunnels - the Queensland experience. *Progress in Aerospace Sciences*, 41(6):471 – 513, 2005. doi: 10.1016/j.paerosci.2005.08.002.

[47] Eric Won Keun Chang, Wilson YK Chan, Keill J Hopkins, Timothy J McIntyre, and Veeraragavan, A. Electrically-heated flat plate testing in a free-piston driven shock tunnel. *Aerospace Science and Technology*, page 105856, 2020.

[48] Peter A. Jacobs, Rowan J. Gollan, Daniel F. Potter, Fabian Zander, David E. Gildfind, P. Blyton, Wilson Y. K. Chan, and Luke Doherty. Estimation of high-enthalpy flow conditions for simple shock and expansion processes using the ESTCj program and library. Technical Report School of Mechanical and Mining Engineering Research Report Number 2011/02, Centre for Hypersonics, The University of Queensland, 2014.

[49] D. L. Schultz and T. V. Jones. Heat transfer measurments in short duration hypersonic facilities. Technical report, AGARDOgraph, 1973.

[50] A. Berezovsky. *Development of thin film heat transfer gauges*. PhD thesis, The University of Queensland, School of Mechanical and Mining Engineering, 1998.

[51] Kevin D. Basore, M. Selzer, Vincent Wheatley, Russell R. Boyce, David John Mee, Bianca R. Capra, Kuhn Markus, and Stefan Briechenk. Performance comparison of distributed injection methods for hypersonic film-cooling. In *20th Australasian Fluid Mechanics Conference*, pages 1–4, 2016.

[52] Dylan J. Wise and Michael K. Smart. Roughness-induced transition of hypervelocity boundary layers. *Journal of Spacecraft and Rockets*, 51(3):847–854, 2014. doi: 10.2514/1.A32674.

[53] Will O. Landsberg, Vincent Wheatley, Michael K. Smart, and Ananthanarayanan Veeraragavan. Enhanced supersonic combustion targeting combustor length reduction in a Mach 12 scramjet. *AIAA Journal*, 56(10):3802–3807, 2018. doi: 10.2514/1.J057417.

[54] Peter A. Jacobs, E Rogers R. Weidner, and R. Bittner. Flow establishment in a generic scramjet combustor. *Journal of Propulsion and Power*, 8(4):890–899, 1992. doi: 10.2514/3.23566.

[55] Byrenn Birch, David Buttsworth, and Fabian Zander. Measurements of freestream density fluctuations in a hypersonic wind tunnel. *Experiments in Fluids*, 61(158), 2020. doi: https://doi.org/10.1007/s00348-020-02992-w.

[56] Eugene Hecht. *Optics*. Addison Wesley, 2002.

[57] A Ramprakash, TJ McIntyre, V Wheatley, and DJ Mee. Performance analysis of fldi technique using turbulent jets. In *IX Australian Conference on Laser Diognostics*, 2019.

[58] Eric Won Keun Chang, Wilson YK Chan, Timothy J McIntyre, and Ananthanarayanan Veeraragavan. Hypersonic shock impingement on a heated flat plate at mach 7 flight enthalpy. *Journal of Fluid Mechanics*, 908(R1), 2021.

[59] Tuncer Cebeci and Peter Bradshaw. *Physical and Computational Aspects of Convective Heat Transfer*. Springer-Verlag, 1984.

[60] Will O. Landsberg, Vincent Wheatley, Michael K. Smart, and Ananthanarayanan Veeraragavan. Performance of high Mach number scramjets - tunnel vs. flight. *Acta Astronautica*, 146:103–110, 2018. doi: 10.1016/j.actaastro.2018.02.031.

[61] Suozhu Wang, Zhenxun Gao, Chunhian Lee, and Juanmian Lei. Large eddy simulation of supersonic boundary layer transition over a flat-plate based on the spatial mode. *Advances in Mechanical Engineering*, 6:350203, jan 2014. doi: 10.1155/2014/350203.

[62] Tuncer Cebeci and Peter Bradshaw. *Physical and Computational Aspects of Convective Heat Transfer*. Springer-Verlag, New York, 2012. doi: 10.1007/978-1-4612-3918-5.